Transverse angular distributions of Drell-Yan dilepton pairs from 8.6 fb^{-1} of $p\bar{p}$ collisions at $\sqrt{s} = 1.96$ TeV at D0

John Beddow

School of Physics and Astronomy
University of Manchester

A thesis submitted to the University of Manchester
for the degree of Master of Science
in the Faculty of Engineering and Physical Sciences

2012

Contents

Final Word Count: 4996

List of Figures

Abstract

The angular distributions of leptons from the decays of Drell-Yan dilepton pairs are studied in 8.6 fb^{-1} of $p\bar{p}$ collisions recorded with the D0 detector at the Fermilab Tevatron collider. Drell-Yan events are often analysed in the Collins-Soper reference frame, which defines two angles, $\phi_{\rm CS}$ and $\theta_{\rm CS}$, in the planes transverse to and along the beam direction respectively. The shape of the $\phi_{\rm CS}$ distribution is measured in bins of the dilepton transverse momentum, using events in the e^+e^- and $\mu^+\mu^-$ decay channels. Predictions from the Monte Carlo program PYTHIA are in good agreement with the data.

Name: John Beddow
University of Manchester, School of Physics and Astronomy
Degree: Master of Science
Title: Transverse angular distributions of Drell-Yan dilepton pairs from 8.6 fb^{-1} of $p\bar{p}$ collisions at $\sqrt{s} = 1.96$ TeV at D0
Date: February 2012

Declaration

No portion of the work referred to in the thesis has been submitted in support of an application for another degree or qualification of this or any other university or other institute of learning.

Copyright

Acknowledgements

Firstly I would like to thank my supervisor, Terry Wyatt and his student Mika Vesterinen for their help and guidance at every step of this analysis. I would also like to thank all the other students with whom I have shared the Manchester D0 office this year. Specific thanks to Pengfei Ding and James Agnew and my sister Yvonne for their help proof reading this thesis.

Finally I would like to thank my Mum and Dad for all their encouragement and understanding this past year.

Chapter 1

Introduction

This analysis aims to measure the transverse angular distributions of dilepton pairs produced by $p\bar{p} \rightarrow Z/\gamma^* \rightarrow e^+e^-X$ and $p\bar{p} \rightarrow Z/\gamma^* \rightarrow \mu^+\mu^-X$ Drell-Yan events after applying a Lorentz boost into the dilepton centre of mass frame. These transverse angular distributions are analysed for Monte Carlo (MC) simulation samples of Drell-Yan[1] events at generator and detector level, where generator level refers to a simulation of the pure physics processes without simulation of detector effects and detector level is created by passing the generator level simulation events through a simulation of the D0 detector. By comparing the generator and detector level distributions, correction factors are calculated which are applied to the distributions from data. These corrected data distributions with corresponding uncertainties are then compared to the generator level Monte Carlo distributions

1.1 Theory

By measuring the transverse angular distributions of Drell-Yan dilepton pairs it is possible to probe the polarisation of the gauge boson (Z/γ^*) and test the underlying production dynamics. This specific analysis looks at the distribution of ϕ_{CS} an angle

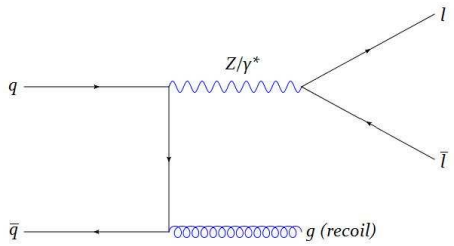

Figure 1.1: Feynman diagram of the signal process, Drell-Yan dilepton production with initial state gluon emission.

in the in the Collins-Soper (CS) centre of mass frame [2]. The CS frame describes a Lorentz boost from the laboratory frame into the dilepton system's centre of mass frame where the two leptons produced from the Z/γ^* decay are back-to-back. The angle ϕ_{CS} is defined as the angle in the CS frame between the plane containing the dilepton system and the plane of the dilepton transverse momentum, p_T^{ll}. Mathematically tan $\phi_{\text{CS}}$is defined as:

$$\tan \phi_{CS} = \frac{\sqrt{M_{ll}^2 + \left(p_T^{ll}\right)^2}}{M_{ll}} \cdot \frac{\vec{\Delta}_r \cdot \hat{R}_T}{\vec{\Delta}_r \cdot \hat{h}} \tag{1.1}$$

where M_{ll} is the dilepton invariant mass, $\vec{\Delta}_r = l - l'$, where l and l' are the respective four-momenta of the particle (electron, muon) and antiparticle (positron, antimuon), $\hat{h}$ is a transverse unit vector in the direction of p_T^{ll} and $\hat{R}_T$ is a transverse unit vector in the direction $\vec{P}_A \times \vec{Q}$ where $\vec{P}_A$ is a vector pointing along the negative z-axis, $\vec{P}_A = (0, 0, -1)$, and $\vec{Q}$ is the four-momentum of the dilepton pair. Figure 1.1 shows a graphical representation of the CS frame.

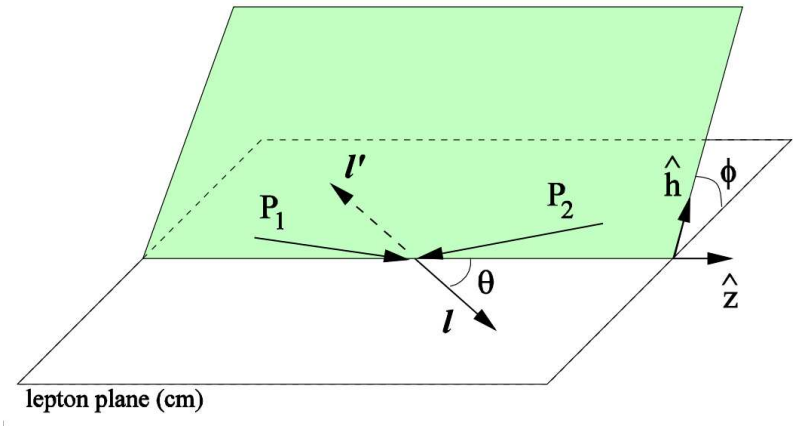

Figure 1.2: Graphical representation of the Collins-Soper frame.

Chapter 2

The D0 Detector

The D0 experiment

The D0 detector is a versatile detector which can be used in the analysis of a wide range of particle physics areas.

As D0 is a well established and long running experiment, several documents exist giving detailed descriptions of all aspects of the experiment. Therefore, this section provides only a brief description of those parts of the D0 detector which are most pertinent to this analysis. Detailed descriptions of the detector can be found in references [3] and [4].

As shown in figure 2.1, which shows a schematic view of the D0 detector, the D0 detector consists of four distinct sections:

- Central tracking system.
- Calorimeter.
- Muon toroid.
- Muon detectors.

The geometry of the detector is defined such that the positive z axis points along the direction of travel of the incoming protons. The angle ϕ describes the azimuthal angle, while the angle θ describes the polar angle measured with respect to the positive z axis. The term rapidity of a particle refers to the quantity, y, defined as $y = \frac{1}{2}\ln\frac{E+p_z c}{E-p_z c}$ where E is the energy of the particle, p_z is the component of the particle's momentum along the z axis and c is the speed of light in a vacuum (299,792,458 m s^{-1}). The pseudorapidity, η, is a quantity similar to y defined as $\eta = -\ln[\tan\frac{\theta}{2}]$. The term transverse momentum, p_T, refers to a particle's momentum transverse to the beam axis defined as $p_T = p\sin\theta$, where p is the particle's momentum.

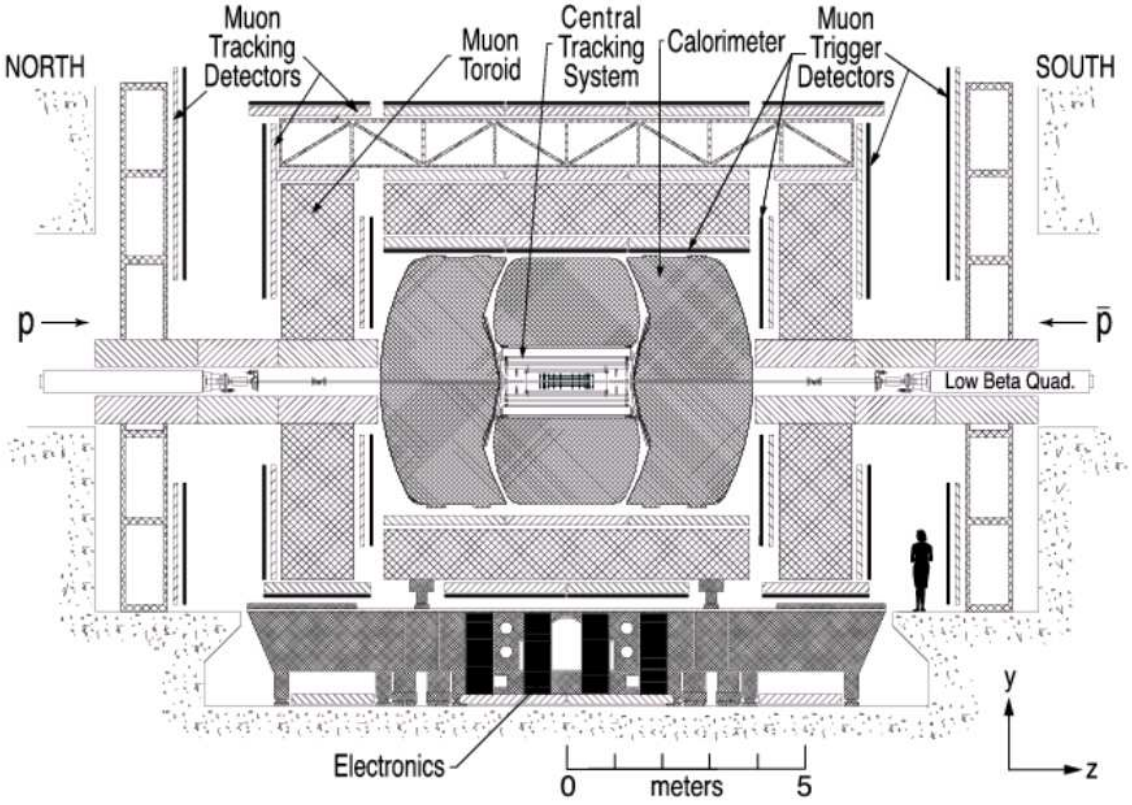

Figure 2.1: Schematic view of the D0 detector. [4]

2.1 Central Tracking System

The central tracking system consists of a silicon microstrip tracker (SMT), a central fiber tracker (CFT) and a solenoidal magnet (field strength approximately 2 T).

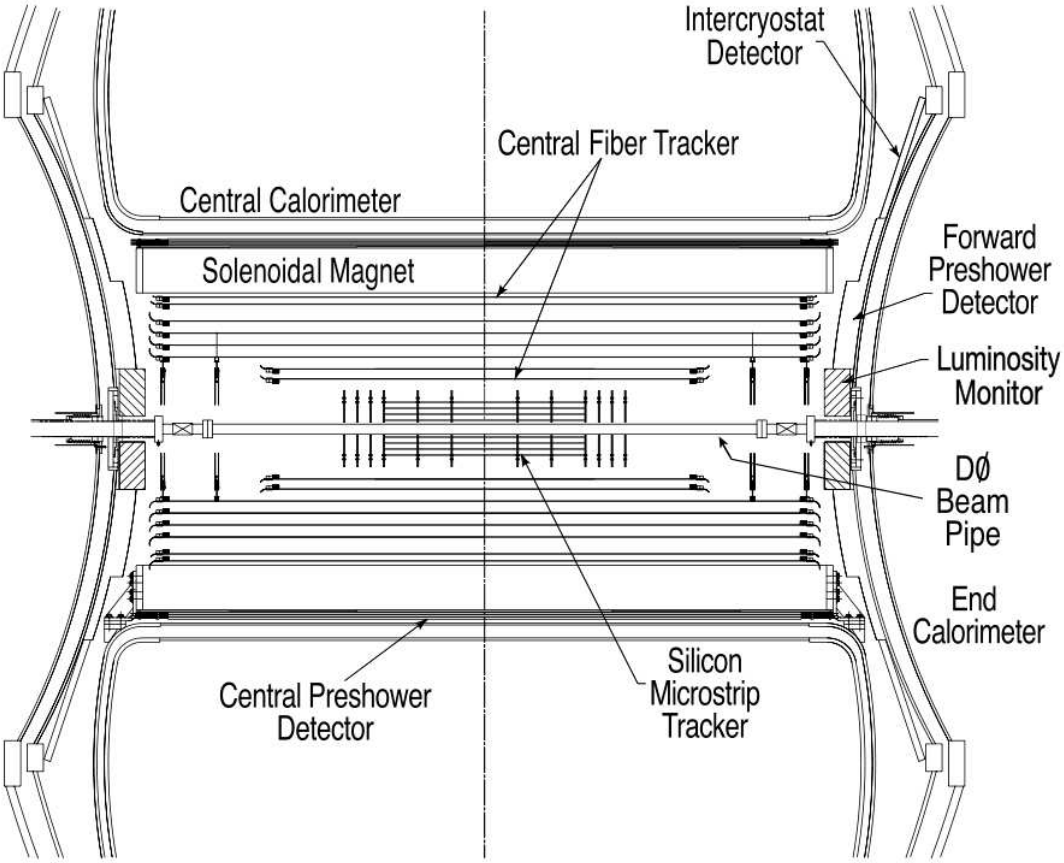

Figure 2.2: Schematic view of the D0 central tracking system [4]

The SMT is the innermost component of the central tracker and is used to detect the tracks of charged particles as well as displaced vertexes from heavy flavour quark decays. The CFT consists of layers of scintillating fibers surrounding the SMT covering a range of $|\eta| < 1.7$ [4]. The CFT provides additional tracking information for the central region of the detector.

The solenoidal magnet bends the paths of charged particles. The curved track of a particle within the magnetic field gives information about it's charge, as oppositely

charged particles curve in opposite directions relative to each other in a magnetic field, and it's momentum from the degree of curvature of the track.

2.2 Calorimeter

The D0 calorimeter is separated into three parts (a central calorimeter (CC) with range of $|\eta| < 1.1$ and two end calorimeters (ECs) which range over $1.5 < |\eta| < 4$) with a small η separation over the range $1.1 < |\eta| < 1.5$ between each part known as the Inter-Calorimeter Region (ICR) which contains some additional detectors which provide some measurement coverage over this region. The calorimeter system consists of an Electromagnetic (EM) Calorimeter and two hadronic calorimeters. Figure 2.3 shows the layout of the D0 calorimeter system.

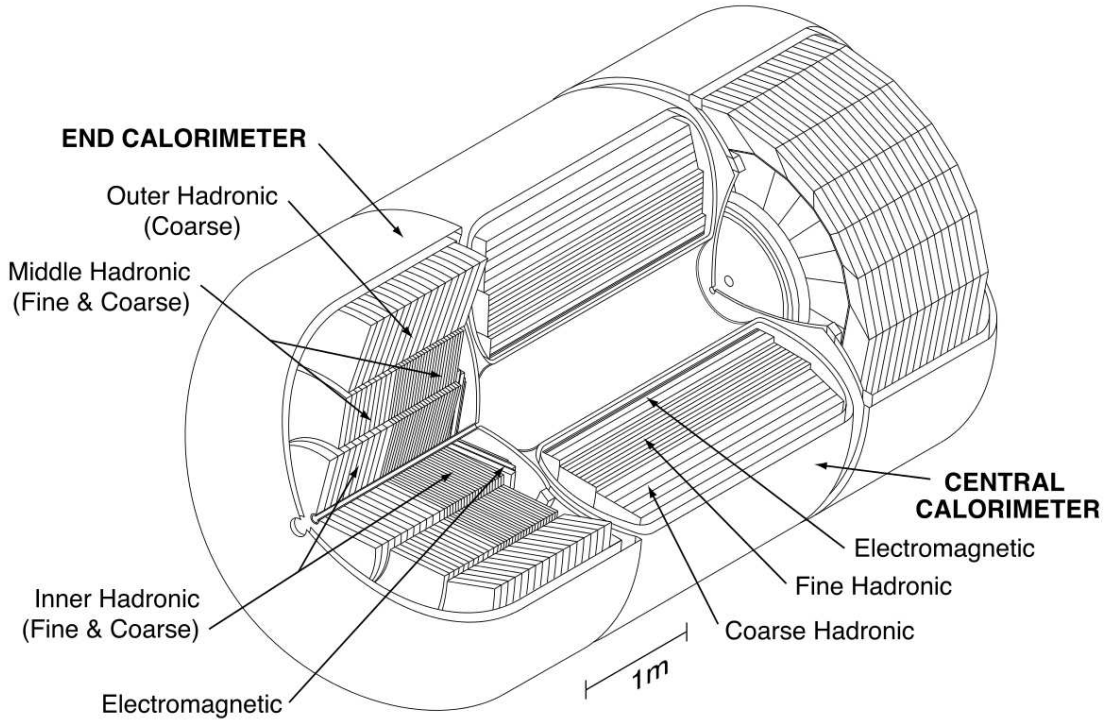

Figure 2.3: Isometric view of the D0 calorimeter system [4]

The EM calorimeter is used in this analysis to identify electrons, muons and photons

and measure the energies of electrons and photons. The EM calorimeter is designed to extend over the typical spatial range of electrons produced in the range over which $p\bar{p}$ collisions occur within the detector.

The two hadronic calorimeters are not especially important for this analysis but detailed information about their functions and designs can be found in references [3] and [4].

2.3 Muon System

The muon detection system at D0 has coverage up to $|\eta| \approx 2$ and consists of (in order of radial distance from the beam axis) muon trigger detectors, a series of muon tracking detectors, an array of toroidal magnets and a further series of muon tracking detectors. The trigger detectors provide timing information about detected muons relative to the measured beam crossing which can be used to discriminate against background processes such as cosmic ray muons in this analysis, this is covered in chapters 3 and 5. The muon toroids produce a magnetic field of strength 1.9-2 T and are used to deflect away from the outer muon detectors long lived particles which pass through all of the EM and hadronic calorimeter systems. The toroidal magnets also help with muon p_T measurements in a similar way to how the solenoid helps with electron p_T measurements with curvature of a muons track being measurable from the different layers of muon tracking detectors before and after the muon toroids. The muon tracking detectors measure the tracks made by muons through the detector as well as measuring muon energies.

Chapter 3

Event Selection

To reduce contamination of the analysis samples with events from background processes, selection requirements are made on various parameters measured by the detector.

3.1 Dielectron events

For dielectron analysis samples events are subject to the following requirements:

- Two leptons of opposite charge in the final state.
- Each lepton with $p_T > 20$ GeV/c. p_Ts are calculated from energy measurements recorded by the calorimeter. This cut helps to eliminate backgrounds such as events from $Z \rightarrow \tau\tau$ decays.
- Each lepton's EM cluster in the calorimeter matched to a corresponding charged particle track in the central tracking system.
- $0.25 < \frac{p_T}{p_T^{\text{track}}} < 4$, where p_T^{track} is the measured p_T of the lepton's track. This is effectively a cut on $\frac{E}{p}$ over the same range and acts to reduce lepton misidenti-

fication.

- $|\eta_{\rm det}| < 3$ for each lepton, where $|\eta_{\rm det}|$ is the pseudorapidity of the lepton as measured from the angle between the axis connecting the location of the lepton's recorded EM cluster in the calorimeter and the centre of the detector, $z = 0$, to the beam axis.

- For leptons in the ICR ($1.1 < |\eta_{\rm det}| < 1.5$) additional selection requirements are made:

  - At least one hit in the SMT.

  - Isolation requirement, lepisohc4<2.5.

  - ICR specific neural network discriminant requirement.

- Leptons outside the ICR are required to have multivariate discriminant lepemv>-0.9.

- $70 < M_{inv}^{ll} < 110$ GeV/c^2, where M_{inv}^{ll} refers to the invariant mass of the dilepton system as calculated by the four vector sum of the invariant masses of the two leptons. Similarly p_T^{ll} is the transverse momentum of the dilepton system calculated from the four vector sum of the p_Ts of each lepton. This selection requirement constricts M_{inv}^{ll} to the region around the invariant mass of the Z boson, M_Z, which removes the majority of dielectron events produced from $\gamma^* \rightarrow e+e-$ decays, leaving a sample of pure Z boson decays.

- $|\Delta z| < 3$, where $|\Delta z| <$ is the separation along the beam axis of the primary vertices of the two leptons.

3.2 Dimuon events

The dimuon analysis requires two oppositely charged leptons in the range $70 < M_{inv}^{ll} < 110$ GeV/c^2 with each lepton having:

- a signal in the muon detector system matched to a track in the central tracking system.
- trkcone/p_T < 0.2, where trkcone is the sum of all the p_Ts of any measured tracks within a certain radius around the muon direction, excluding the p_T of the muon itself. This cut helps to distinguish muons from jets as jets shower in the detector which typically means their p_T distribution is much less focussed than that for a real muon. A similar requirement is made on the sum of measured energies of EM clusters surrounding the muon's direction in the muon calorimeter.
- lepton $p_T > 15$ GeV/c.
- At least one hit in the SMT.
- track $\chi^2 < 4$, where track χ^2 is a measure of the χ^2 value for the fit applied to the measured hits from a particle in the central tracking system by the track fitting algorithm. A large track χ^2 value indicates that the measured track doesn't fit very accurately to the specific helical shape that the fitting algorithm searches for. Large track χ^2 values often come from background processes such as the decays of particles with short lifetimes (for instance $K \rightarrow \mu\nu$) within the central tracking system.
- $|\eta_{\rm det}| < 2$, this is the limit of detector's range of measurement for muons.

To eliminate the background from cosmic ray muons, $\mu^{\rm cos}$, events are required to pass a combined selection cut comprising of cuts on scintillator timing , DCA (distance of closest approach) and collinearity of the two lepton tracks.

Chapter 4

Monte Carlo Simulation

For this analysis, PYTHIA generator level Monte Carlo (MC) samples (RESBOS[6] with CTEQ 6.6 [10] parton distribution functions (PDFs), PYTHIA[5] with CTEQ 6L1 [11] PDFs, HERWIG++[7] and POWHEG[8]) and one full detector simulation Monte Carlo sample (PYTHIA) were used. All four generator MC samples simulate final state radiation (FSR) for each event, however in the dielectron channel, only PYTHIA and RESBOS generator MC samples merge photons from final state bremsstrahlung back into the measurements of electrons, this option is not chosen for the HERWIG++ and POWHEG samples used in this analysis. Merging of final state photons at generator level is desirable as it removes the necessity to correct for this process later in the analysis which would increase systematic uncertainties on any measurements.

To create the PYTHIA detector MC sample, the PYTHIA generator level sample events are passed through a GEANT[9] based simulation which models the response of the D0 detector. Additional data events from randomly triggered bunch crossings are merged with the MC sample to mimic extra $p\bar{p}$ collisions within the same bunch crossing. Detector MC events are treated in exactly the same way as events from the data sample.

4.1 Corrections to Monte Carlo

Certain issues exist which cause the PYTHIA simulation to be inaccurate in aspects of both physics and detector reconstruction. There are three main issues with PYTHIA MC simulation which need to be addressed: that the shape of the Z/γ^* p_T distribution at propagator level is less accurately simulated by PYTHIA when compared to RESBOS; that the efficiencies for reconstructing electrons and muons are overestimated when compared to the measured efficiencies of the detector from experimental data; and that the detector's p_T resolution for muons and energy resolution for electrons are also overestimated by the simulation.

4.1.1 RESBOS reweighting

To improve the simulated Z/γ^* p_T, p_T^Z, distribution the PYTHIA p_T^Z distribution is reweighted at generator level to match the distribution in RESBOS. To do this, two-dimensional histograms of propagator, or "truth", level Z boson p_T, $p_T^{Z^{true}}$, and Z rapidity, y_Z^{true}, are made for both PYTHIA and RESBOS generator MC samples, where propagator level refers to measurements made of Z boson properties before the Z has decayed. In reality it is impossible to measure any properties of the Z boson at this level however the PYTHIA and RESBOS generator level MC samples contain these variables which can be used to the benefit of this analysis.

A histogram of the ratio of PYTHIA to RESBOS is produced by dividing the RESBOS 2D histogram by the equivalent for PYTHIA, as shown in figures 4.1a and 4.1b. The reweighting is applied to the PYTHIA signal MC samples at generator and detector level by accessing the $p_T^{Z^{true}}$ and y_Z^{true} values for each event and multiplying the event weight by the content of the ratio histogram bin corresponding to these values.

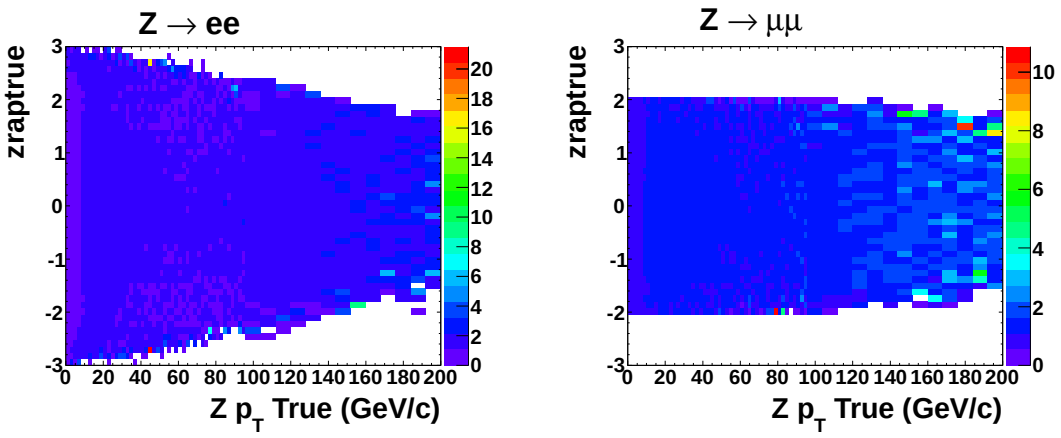

(a) Dielectron p_T ratio

(b) Dimuon p_T ratio

Figure 4.1: Histograms to reweight PYTHIA events to match RESBOS $p_T^{Z^{true}}$ and y_Z^{true} distributions for dielectron and dimuon analysis.

Figures 4.2a to 4.3d show the distributions for various "truth" level variables for RESBOS and PYTHIA generator level MC after RESBOS reweighting is applied to PYTHIA. Plots are normalised to unit area with vertical axes measured in dN/N, where N is the integral of each distribution.

As a result of reweighting PYTHIA to RESBOS in $p_T^{Z^{true}}$ and y_Z^{true}, the propagator level distributions for the two samples are identical for $p_T^{Z^{true}}$ and y_Z^{true} as expected in both dielectron and dimuon samples. Slight differences exist between the propagator dilepton invariant mass, M_{ll}^{true}, distributions for PYTHIA and RESBOS however the differences between the distributions of these two are small compared to the difference between either generator and the distribution from POWHEG. This large difference in shape is caused by POWHEG not merging final state photon emission back into lepton reconstruction as is done for PYTHIA and RESBOS.

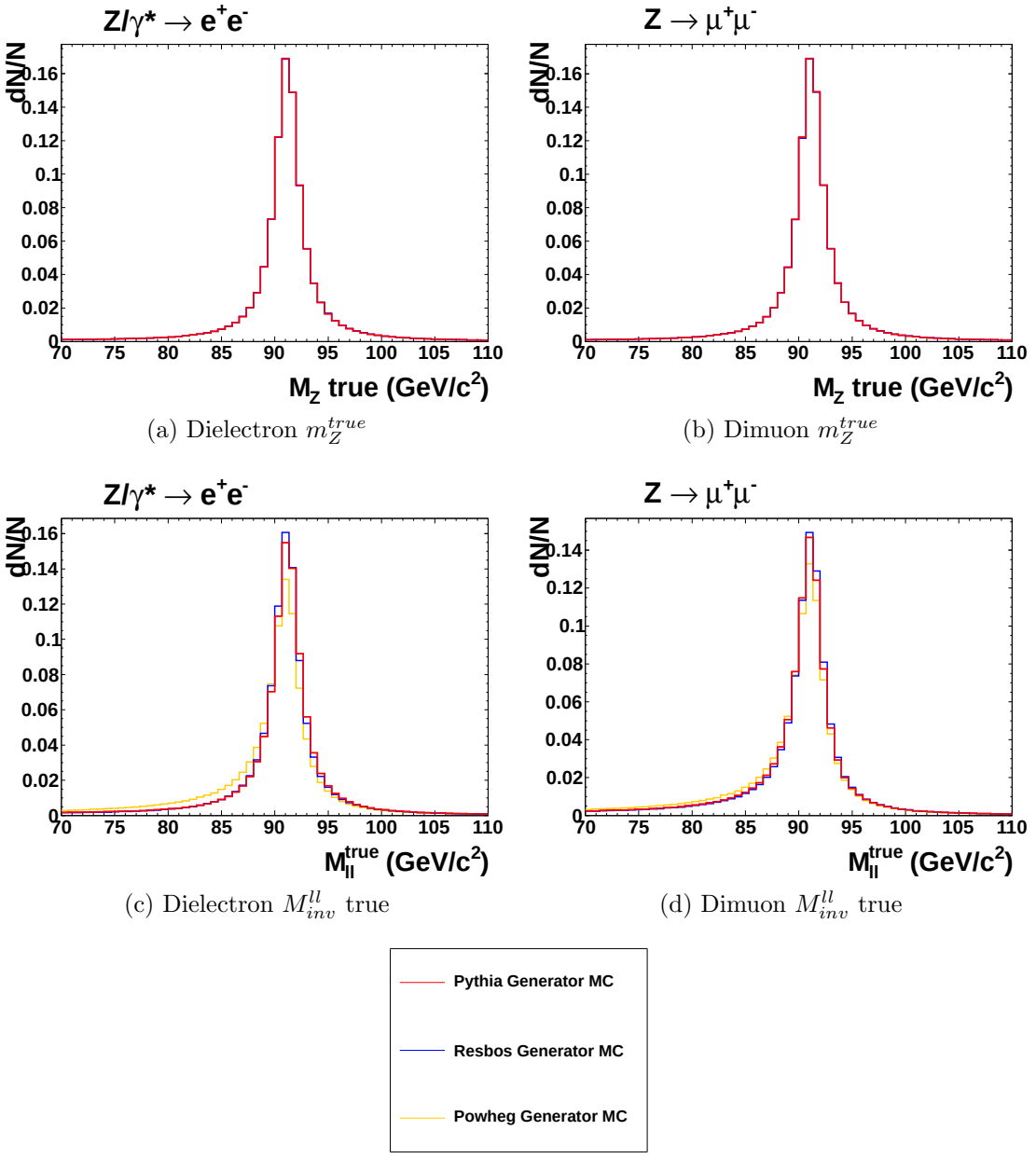

(a) Dielectron m_Z^{true}

(b) Dimuon m_Z^{true}

(c) Dielectron M_{inv}^{ll} true

(d) Dimuon M_{inv}^{ll} true

Figure 4.2: Dielectron and dimuon Monte Carlo propagator level Z boson invariant mass distributions for RESBOS generator MC and PYTHIA generator MC with RESBOS reweighting applied. And dielectron and dimuon Monte Carlo propagator level dilepton invariant mass distributions for RESBOS, PYTHIA with RESBOS reweighting applied and POWHEG generator MC samples

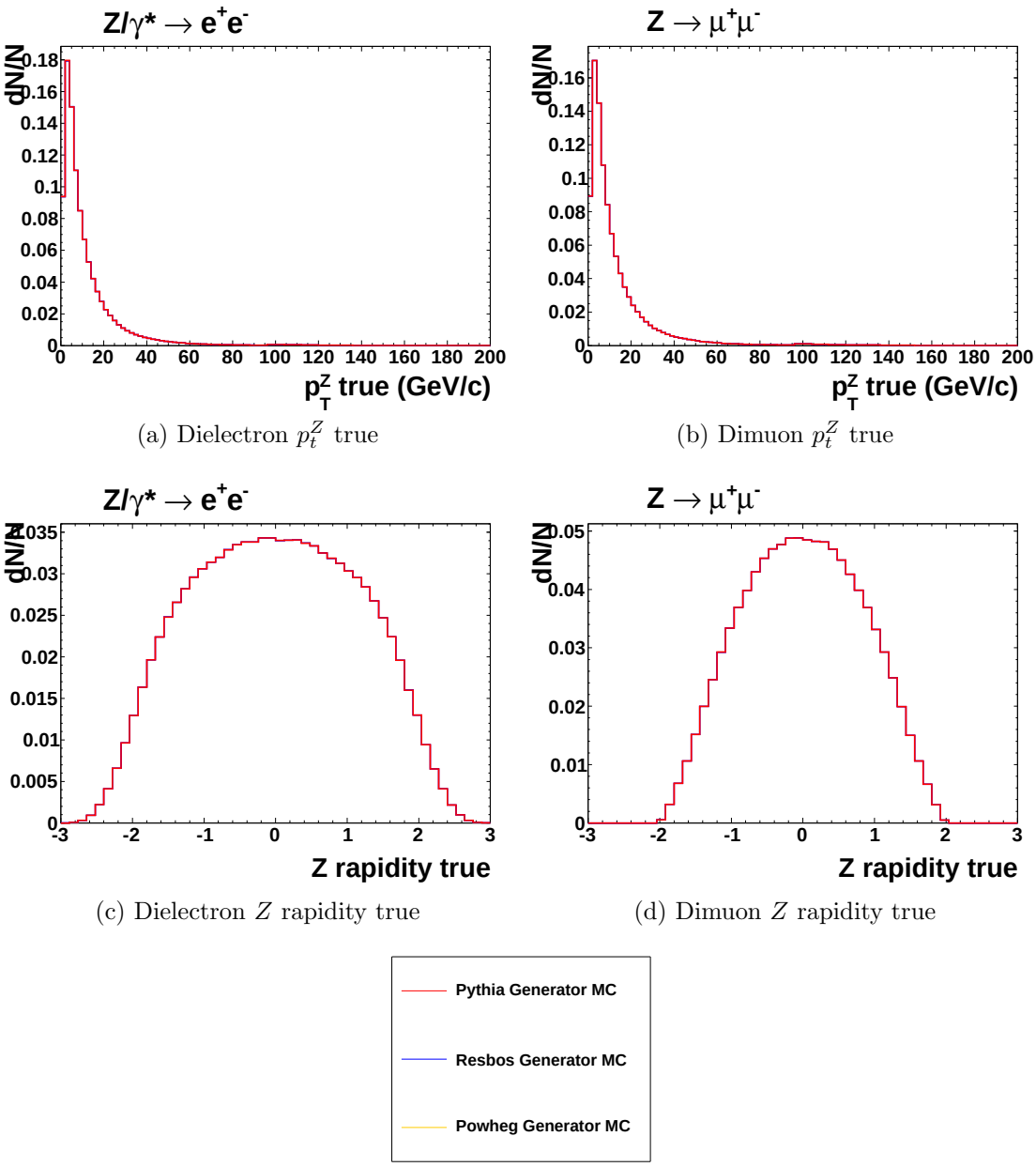

(a) Dielectron p_t^Z true

(b) Dimuon p_t^Z true

(c) Dielectron Z rapidity true

(d) Dimuon Z rapidity true

Figure 4.3: RESBOS and PYTHIA generator MC "truth" level distributions of p_T^Z and Z rapidity for dielectron and dimuon samples. RESBOS reweighting applied to PYTHIA.

4.1.2 Tracking Efficiency Corrections

Due to the geometry of the detector and the fact that at various times certain parts of the detector may be broken or not functioning at 100% efficiency, the tracking efficiency varies across the detector. When compared to the tracking efficiency measured from detector data, the detector MC simulation of tracking efficiency is seen to be poorly modeled.

To correct for the tracking efficiency issues, a correction is applied to MC events to compensate for the differences in track matching efficiency between data and MC. To calculate the required corrections, histograms of tracking efficiency are made separately for electrons and muons in both data and detector MC. For electrons, a tracking efficiency histogram is made by performing a tag and probe analysis on a sample of dielectron events. In a tag and probe analysis a candidate electron is required which fired the level 3 trigger of the detector and has a measured track in the central tracker matched to a corresponding EM cluster in the calorimeter, this is termed the "tag" electron. To find the "probe" electron, a corresponding EM cluster is searched for in the opposite half of the detector from the tag electron. The invariant mass of the dielectron system is then calculated from the two EM clusters and confirmed to be within the region of M_Z to verify that the event is from a true dielectron decay. The tracking efficiency with respect to a specific variable is then calculated by plotting histograms of that variable for the probe electrons in two cases: firstly, the distribution for the entire sample; and then the distribution only for events in the sample where the probe electron has a measured track matched to its EM cluster. Comparing the two histograms allows a calculation of the electron tracking efficiency to be made. An equivalent method is used to measure muon tracking efficiencies by using a sample of dimuon events and requiring hits in the muon system of the detector.

In this analysis, the tracking efficiencies are measured as a function of ϕ, $\eta_{detector}$ and

z and combined into a three dimensional histogram. To calculate the tracking efficiency correction required for detector MC, a histogram is made of the measured detector tracking efficiency as a result of a tag and probe analysis performed on experimental data. The values of ϕ, $\eta_{detector}$ and z for each lepton in the detector MC sample are fed into this tracking efficiency histogram and the lepton is given a tracking efficiency probability value corresponding to the content of the histogram bin for these three values. A uniform random number is generated for each lepton and the event is omitted if this random number is greater than the lepton's tracking efficiency probability.

4.1.3 Constraints to Z Mass

Following a preliminary analysis of ϕ_{CS} a further correction to the analysis was introduced to improve bin purities for ϕ_{CS} and p_T^{ll} distributions for both dielectron and dimuon analysis. This is particularly needed for dimuon analysis where nominal ϕ_{CS} and p_T^{ll} bin purities are too low.

The term bin purity, for a given distribution, refers to a measure of how events in MC migrate between bins in the distribution when detector simulation is applied to generator level MC events. A distribution with high bin purity contains a large proportion of events where MC events fall into the same bin in the distribution at generator level and detector level.

To measure the bin purities in ϕ_{CS} and p_T^{ll}, as shown in figures 4.4a to 4.4f, two histograms are filled: one filled with the generator level MC distribution; the other is also filled with the generator level distribution, but only generator level events which fall into the same histogram bin as the corresponding events from the detector MC sample. Dividing the second histogram by the first gives the bin purity distribution for ϕ_{CS} and p_T^{ll}.

Figures 4.4a and 4.4b show the bin purities for nominal ϕ_{CS} and p_T^{ll}distributions for detector level MC, with 10 bins in ϕ_{CS}. Figures 4.4c and 4.4d show the same distributions only now with 5 bins in ϕ_{CS}, this shows an overall improvement in ϕ_{CS} bin purity for both the dielectron and dimuon samples. However it is still possible to improve bin purities further, especially for the dimuon samples.

To further improve the bin purities, an attempt is made to constrain the individual lepton p_Ts to M_Z at detector level for both MC and data. Constraining to M_Z attempts to push events that at generator/physics level have $M_{inv}^{ll} \approx M_Z$ but have been smeared away from the Z pole by detector resolution effects back towards the peak of the M_Z distribution. To perform the constraint, an iterative process modifies the detector level transverse momenta values of the two leptons

$$p_T^{i'} = p_T^i + \tau_i \times \sigma_{p_T^i},\ i = 1, 2 \tag{4.1}$$

where $p_T^{i'}$ is the modified lepton p_T, $\sigma_{p_T^i}$ is the uncertainty on p_T and τ_i is the step size of the variation of p_T. From these new transverse momenta, a new value of M_{inv}^{ll} is calculated and a χ^2 value is then calculated from the difference between this reconstructed M_{inv}^{ll} value and the "true" Z boson invariant mass

$$\chi^2 = \left(\frac{m_{ll}^{\text{const}} - M_Z^{\text{true}}}{\Gamma(Z)} \right)^2 + \tau_1^2 + \tau_2^2 \tag{4.2}$$

where M_Z^{true} is the mass of the Z boson, 91.19 GeV/c^2, and $\Gamma(Z)$ is the width of the Z boson, 2.5 GeV/c^2. The values of $\tau_{1,2}$ are varied until the measured χ^2 value reaches a minimum value, the modified lepton p_Ts corresponding to these values of $\tau_{1,2}$ are then used to calculate the M_Z constrained p_T^{ll} and ϕ_{CS} distributions.

Figures 4.4e and 4.4f show the bin purities for ϕ_{CS} and p_T^{ll} with the M_Z constraint applied and show an overall improvement in bin purities in p_T^{ll} and $\phi_{\text{CS}}$for both dielectron

and dimuon samples.

Figures 4.5a to 4.5g and 4.6a to 4.6g show the correlation between generator level and detector level MC dimuon p_T^{ll} distributions before and after the constraint to M_Z is applied for the dimuon detector MC sample. Comparison between the two sets of plots clearly shows an improvement in the correlation between generator level and detector level p_T^{ll} correlation with the M_Z constraint applied.

Figures 4.7a to 4.7g and 4.7a to 4.7g show the correlation between the PYTHIA generator level MC and detector level MC ϕ_{cs} distributions with the constraint to M_Z applied for dielectron and dimuon samples respectively. From comparing the two sets of distributions, it is clear that the resolution for electron ϕ_{cs} measurement is much better than for muons.

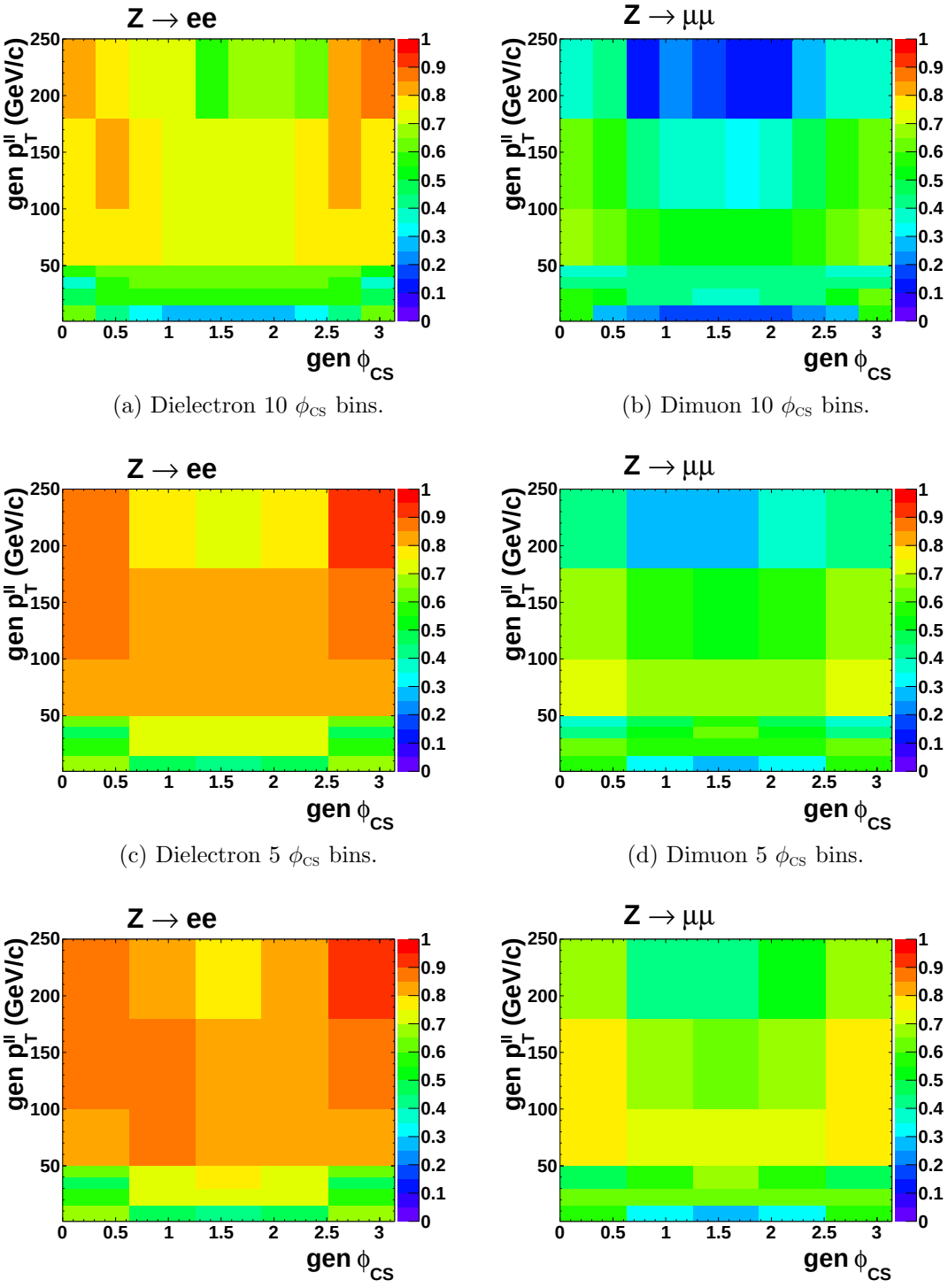

(a) Dielectron 10 ϕ_{CS} bins.

(b) Dimuon 10 ϕ_{CS} bins.

(c) Dielectron 5 ϕ_{CS} bins.

(d) Dimuon 5 ϕ_{CS} bins.

(e) Dielectron 5 ϕ_{CS} bins.

(f) Dimuon 5 ϕ_{CS} bins.

Figure 4.4: Bin purities in ϕ_{CS} and p_T^{ll} for PYTHIA dielectron and dimuon MC samples with and without constraint to Z boson mass.

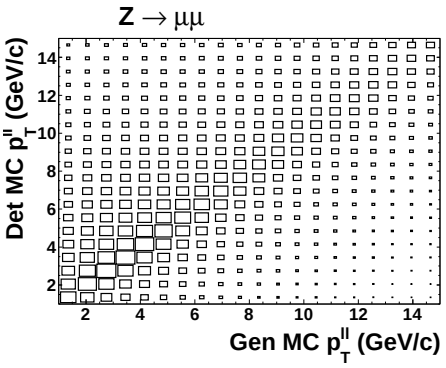

(a) $1 < p_T^{ll} < 15$ GeV/c

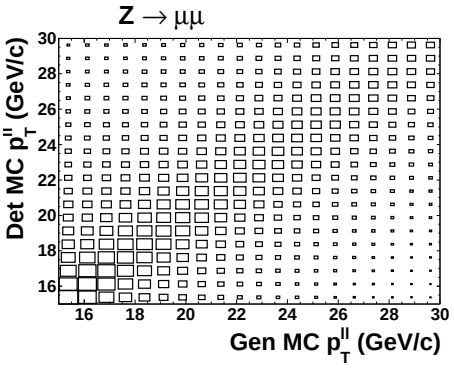

(b) $15 < p_T^{ll} < 30$ GeV/c

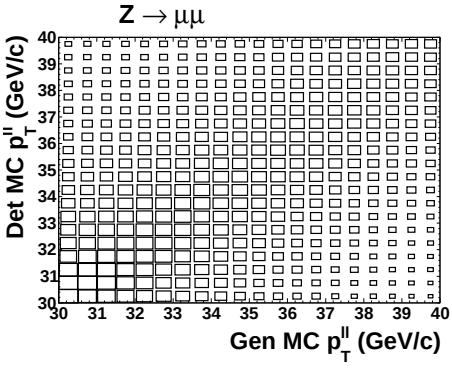

(c) $30 < p_T^{ll} < 40$ GeV/c

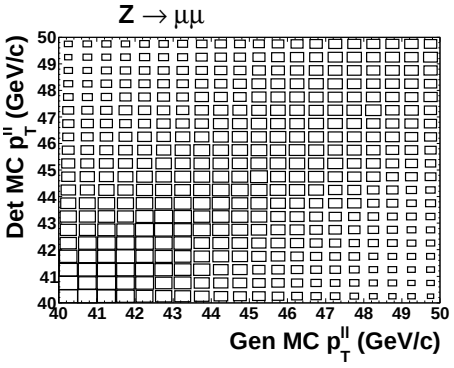

(d) $40 < p_T^{ll} < 50$ GeV/c

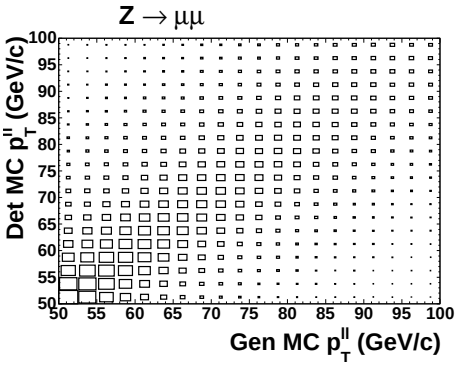

(e) $50 < p_T^{ll} < 100$ GeV/c

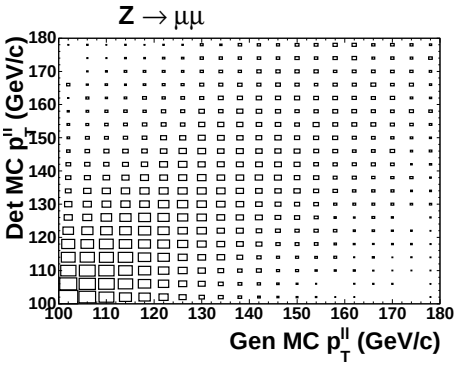

(f) $100 < p_T^{ll} < 180$ GeV/c

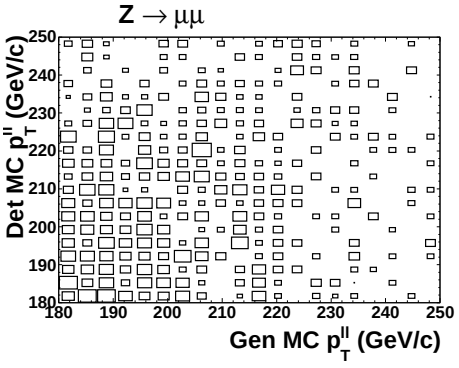

(g) $p_T^{ll} > 180$ GeV/c

Figure 4.5: Scatter plots showing the correlation between generator and detector level MC dimuon p_T^{ll} distributions within selection cuts. Plots binned in detector level p_T^{ll}

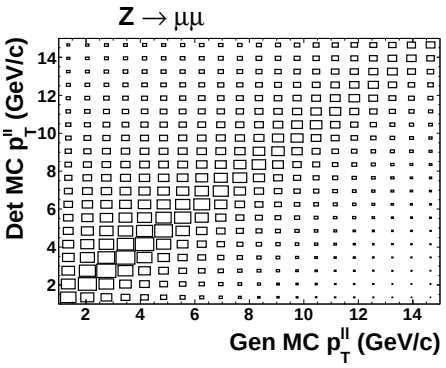

(a) $1 < p_T^{ll} < 15$ GeV/c

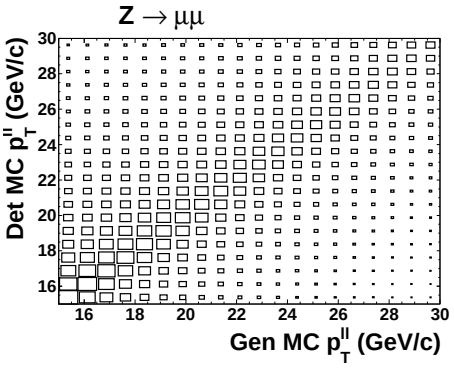

(b) $15 < p_T^{ll} < 30$ GeV/c

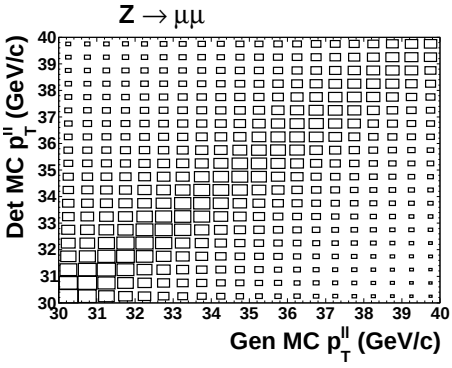

(c) $30 < p_T^{ll} < 40$ GeV/c

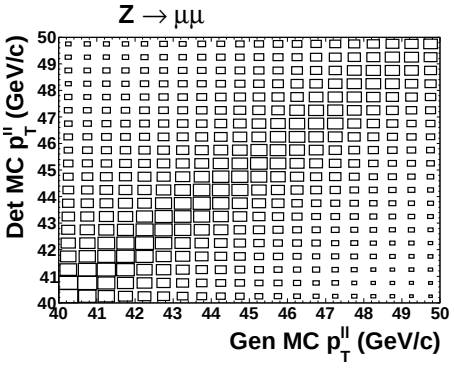

(d) $40 < p_T^{ll} < 50$ GeV/c

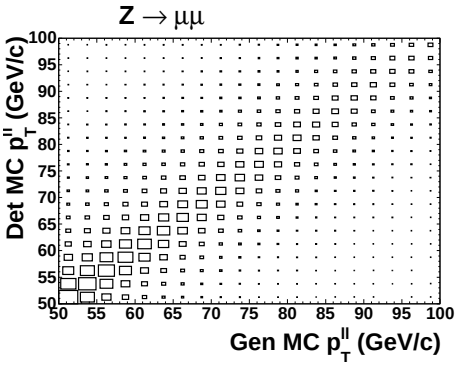

(e) $50 < p_T^{ll} < 100$ GeV/c

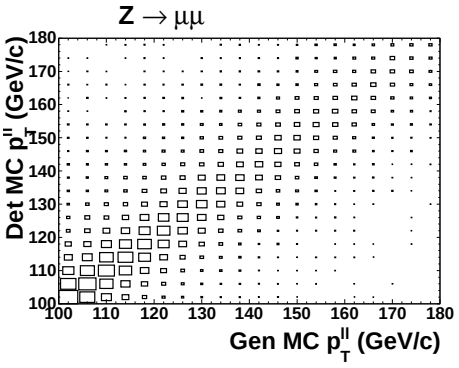

(f) $100 < p_T^{ll} < 180$ GeV/c

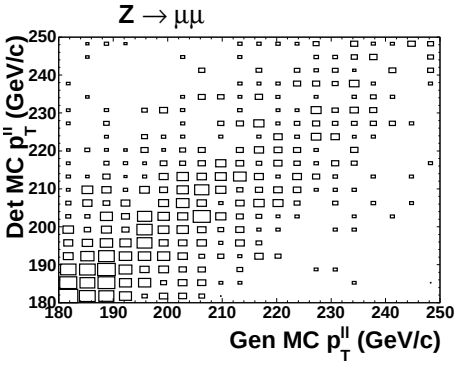

(g) $p_T^{ll} > 180$ GeV/c

Figure 4.6: Scatter plots showing correlation between generator and detector level MC dimuon p_T^{ll} distributions within selection cuts with Z mass constraint applied. Plots binned in detector level M_Z constrained p_T^{ll}

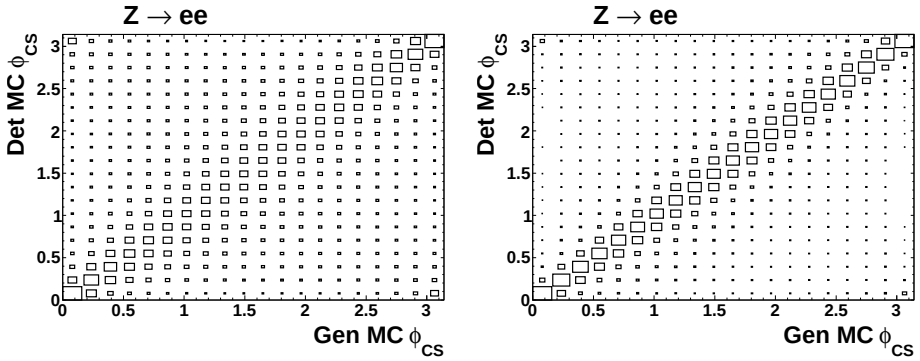

(a) $1 < p_T^{ll} < 15$ GeV/c

(b) $15 < p_T^{ll} < 30$ GeV/c

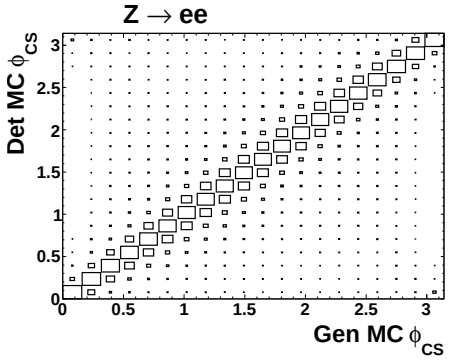

(c) $30 < p_T^{ll} < 40$ GeV/c

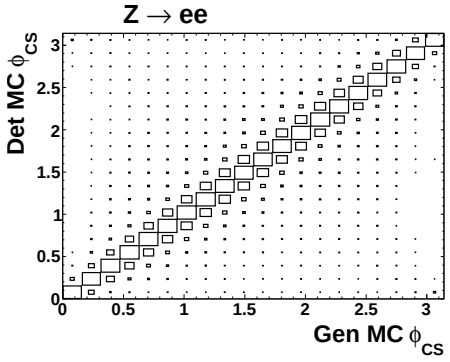

(d) $40 < p_T^{ll} < 50$ GeV/c

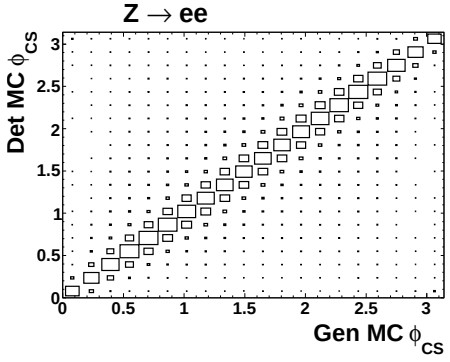

(e) $50 < p_T^{ll} < 100$ GeV/c

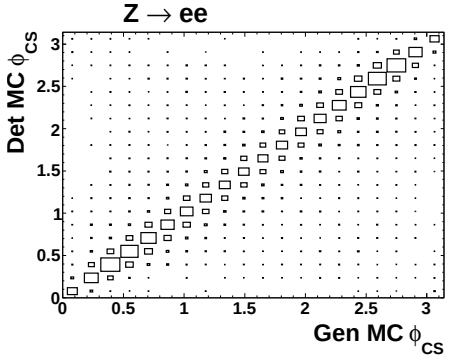

(f) $100 < p_T^{ll} < 180$ GeV/c

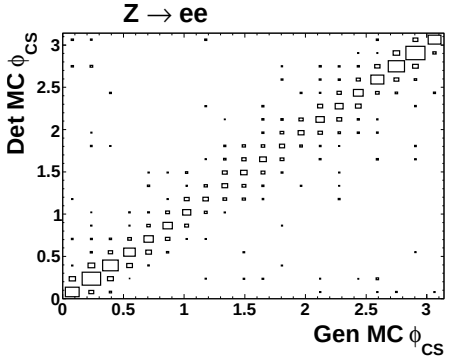

(g) $p_T^{ll} > 180$ GeV/c

Figure 4.7: Correlation between generator and detector level MC dielectron $\phi_{\rm CS}$ distributions within selection cuts with M_Z constraint applied. Plots binned in M_Z constrained detector level p_T^{ll}

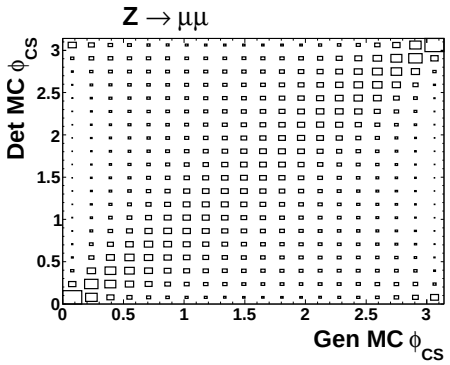

(a) $1 < p_T^{ll} < 15$ GeV/c

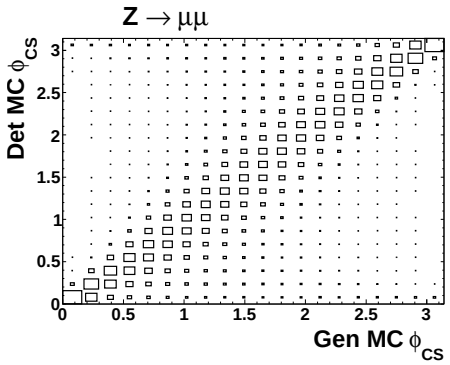

(b) $15 < p_T^{ll} < 30$ GeV/c

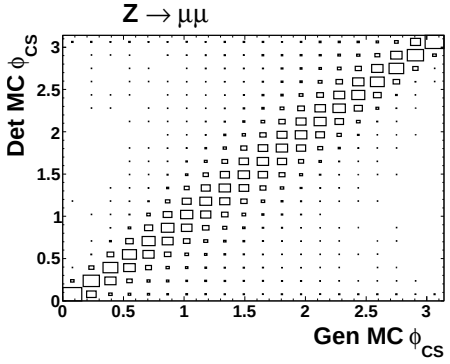

(c) $30 < p_T^{ll} < 40$ GeV/c

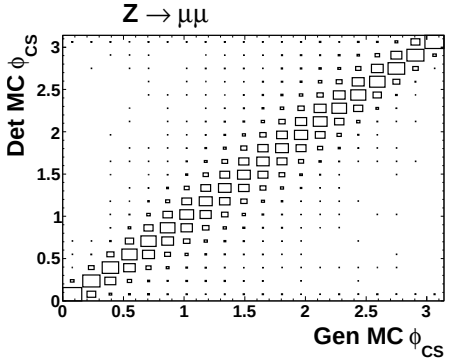

(d) $40 < p_T^{ll} < 50$ GeV/c

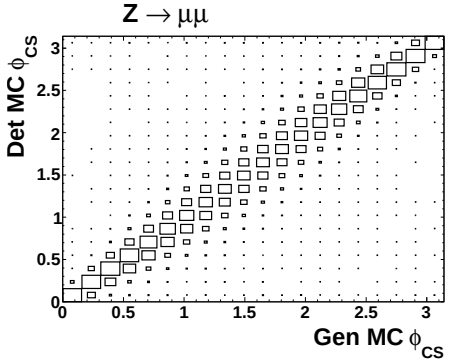

(e) $50 < p_T^{ll} < 100$ GeV/c

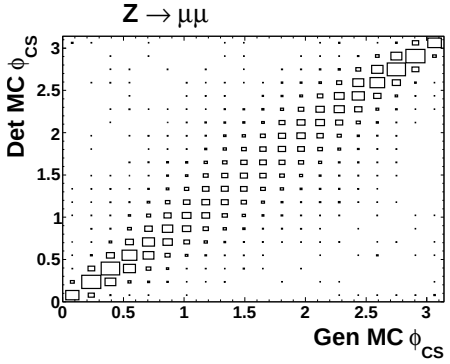

(f) $100 < p_T^{ll} < 180$ GeV/c

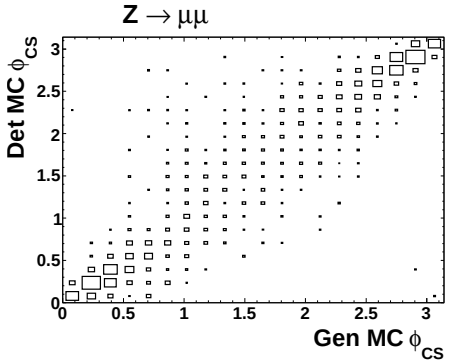

(g) $p_T^{ll} > 180$ GeV/c

Figure 4.8: Correlation between generator and detector level MC dimuon $\phi_{\rm CS}$ distributions within selection cuts with M_Z constraint applied. Plots binned in M_Z constrained detector level p_T^{ll}

4.2 Generator MC Comparisons

Selection cuts on dielectron generator MC require that:

- $70 < M_{e^+e^-} < 110$ GeV/c^2.
- lepton $p_T > 20$ GeV/c.
- lepton $|\eta| < 3$.

While dimuon generator MC events require:

- $70 < M_{\mu\mu} < 110$ GeV/c^2.
- lepton $p_T > 15$ GeV/c.
- lepton $|\eta| < 2$.

these selection requirements are made to mimic the cuts made on these variables at detector level so that comparisons can be made between generator level MC and detector level samples (MC and data).

Figures 4.9a to 4.12g show the distributions of positive and negative lepton p_T, η, p_T^{ll}, M_{inv}^{ll} and ϕ_{CS} for each generator MC dielectron (dimuon) sample compared to PYTHIA dielectron (dimuon) detector MC.

All four generator MC samples show a similar shape for individual lepton $p_T$and η in both dielectron and dimuon samples. The p_T^{ll} and M_{inv}^{ll} distributions however show differences between PYTHIA and RESBOS samples compared to the HERWIG++ and POWHEGdistributions. Again, this is as a result of the HERWIG++ and POWHEG samples not merging final state photons.

Figures 4.11a to 4.12g show the ϕ_{CS} distributions for dielectron and dimuon generator MC samples in bins of p_T^{ll}. The distributions of ϕ_{CS} for dielectron samples show large differences in shape between different generators at low p_T^{ll}($p_T^{ll}<$ 30 GeV/c) with

POWHEG and HERWIG++ having a similarly shaped distributions which are much different from the shape of the PYTHIA and RESBOS distributions caused again by differences in how the generators treat final state photon emission. Also of note is the difference in shape between PYTHIA generator and detector level distributions at low p_T^{ll} for both the dielectron and dimuon samples. This suggests that large correction factors will be required in these bins to compare data to MC.

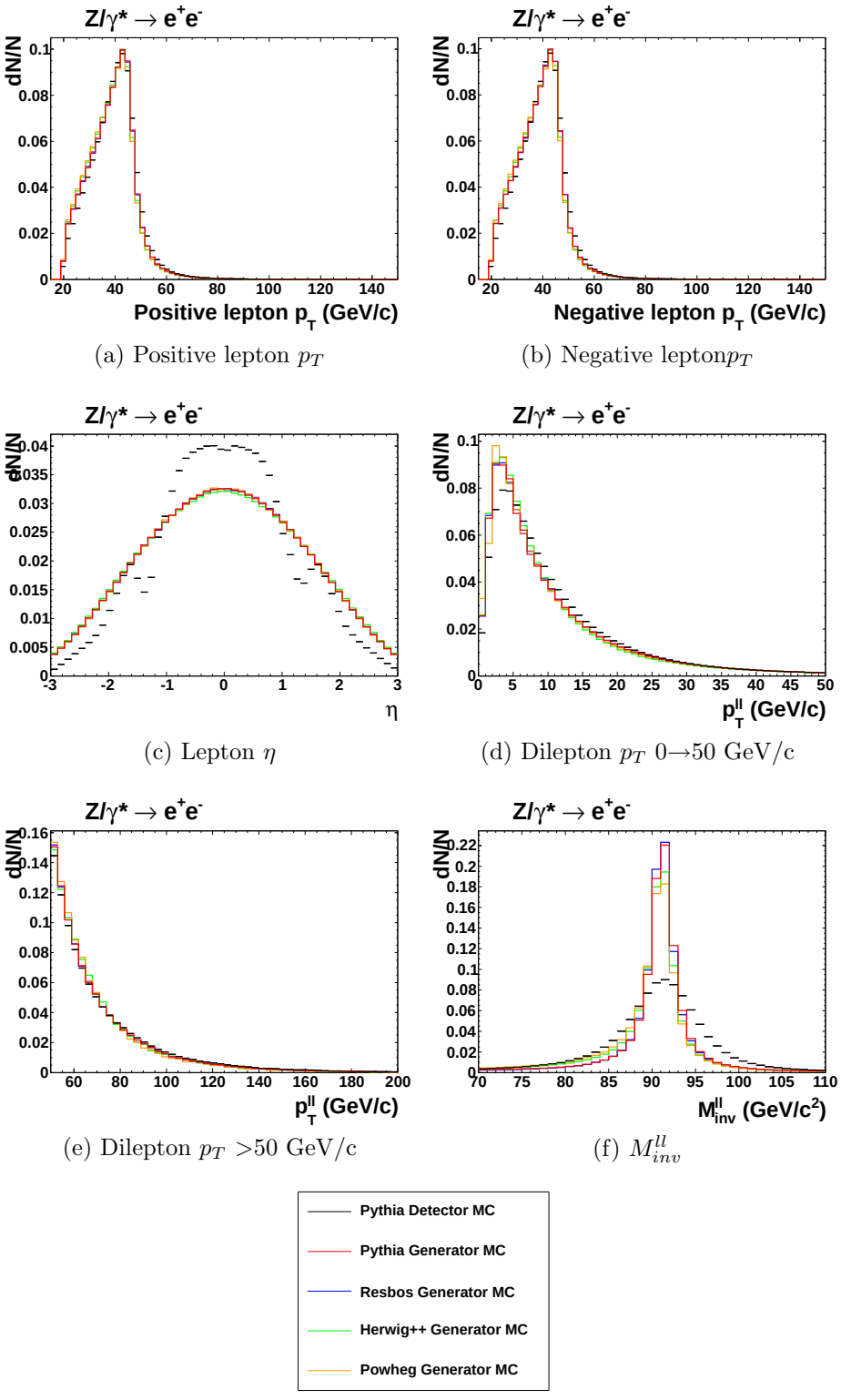

(a) Positive lepton p_T

(b) Negative leptonp_T

(c) Lepton η

(d) Dilepton p_T 0→50 GeV/c

(e) Dilepton p_T >50 GeV/c

(f) M_{inv}^{ll}

Figure 4.9: p_T, η, p_T^{ll} and M_{inv}^{ll} distributions for dielectron PYTHIA, RESBOS, POWHEG and HERWIG++ generator MC samples compared to PYTHIA detector MC.

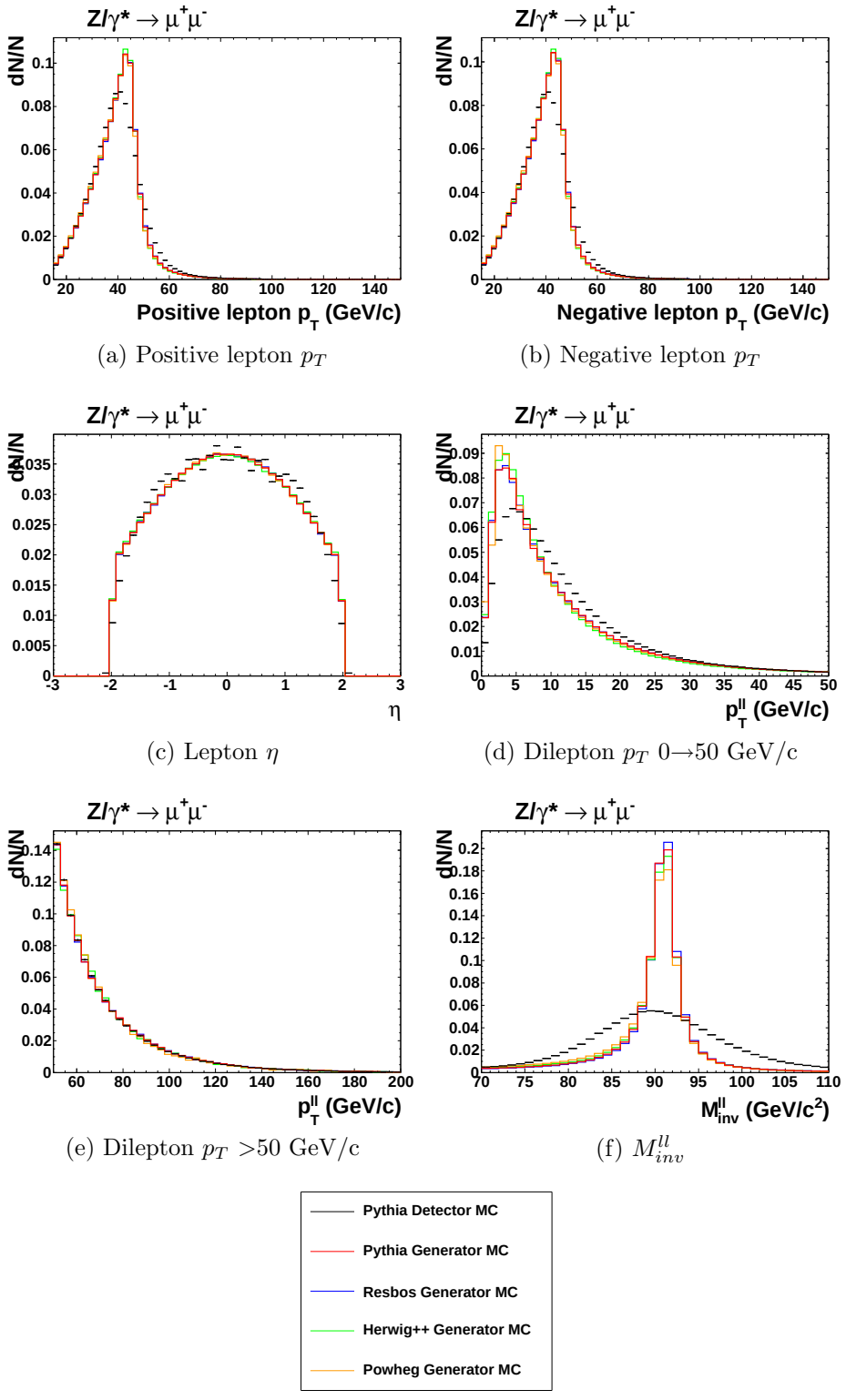

(a) Positive lepton p_T

(b) Negative lepton p_T

(c) Lepton η

(d) Dilepton p_T 0→50 GeV/c

(e) Dilepton p_T >50 GeV/c

(f) M_{inv}^{ll}

Figure 4.10: p_T, η, p_T^{ll} and M_{inv}^{ll} distributions for dimuon PYTHIA, RESBOS, POWHEG and HERWIG++ generator MC samples compared to PYTHIA detector MC.

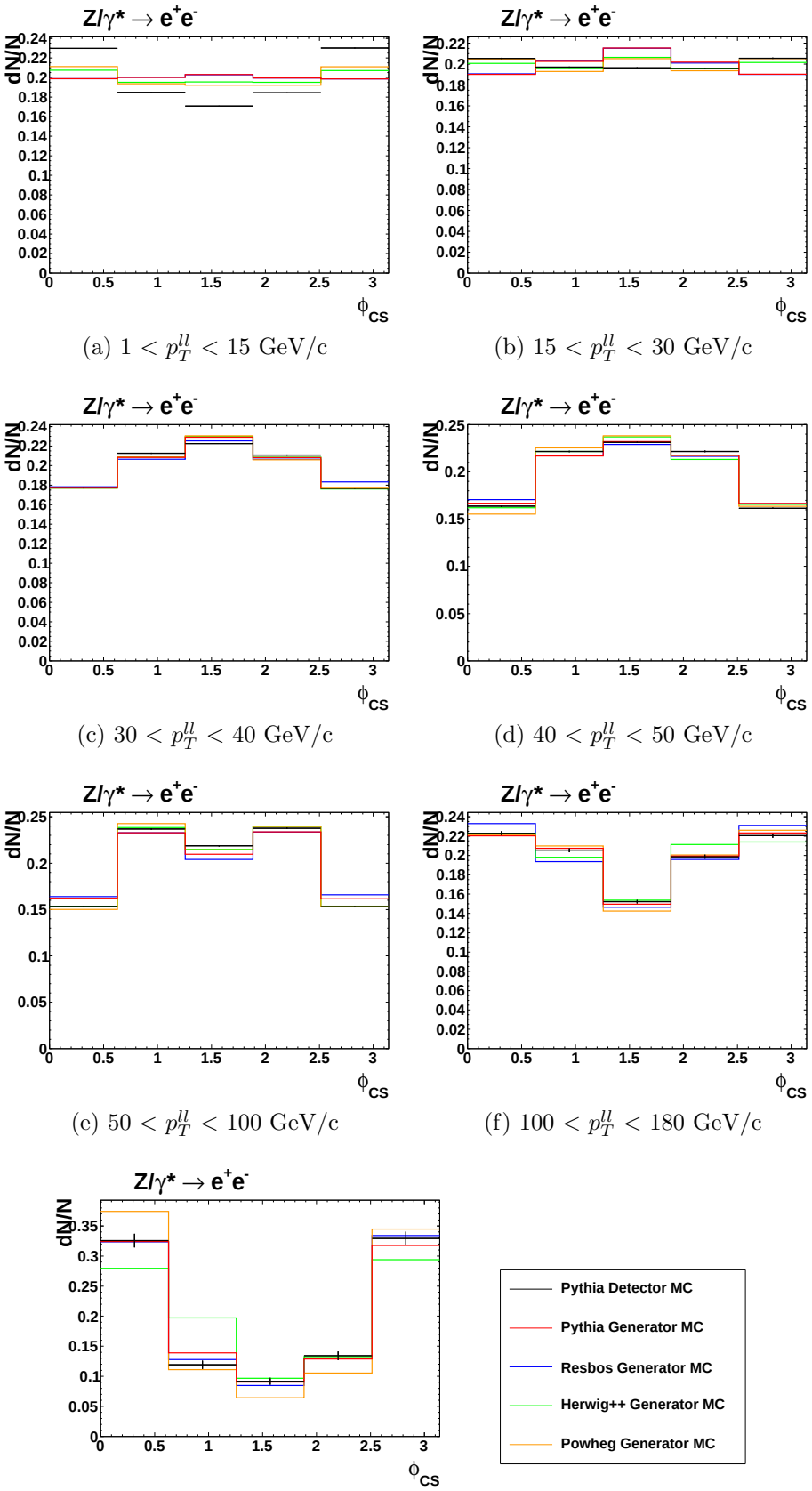

(a) $1 < p_T^{ll} < 15$ GeV/c

(b) $15 < p_T^{ll} < 30$ GeV/c

(c) $30 < p_T^{ll} < 40$ GeV/c

(d) $40 < p_T^{ll} < 50$ GeV/c

(e) $50 < p_T^{ll} < 100$ GeV/c

(f) $100 < p_T^{ll} < 180$ GeV/c

(g) $p_T^{ll} > 180$ GeV/c

Figure 4.11: ϕ_{CS} distributions for dielectron PYTHIA, RESBOS, POWHEG and HERWIG++ generator MC samples compared to PYTHIA detector MC.

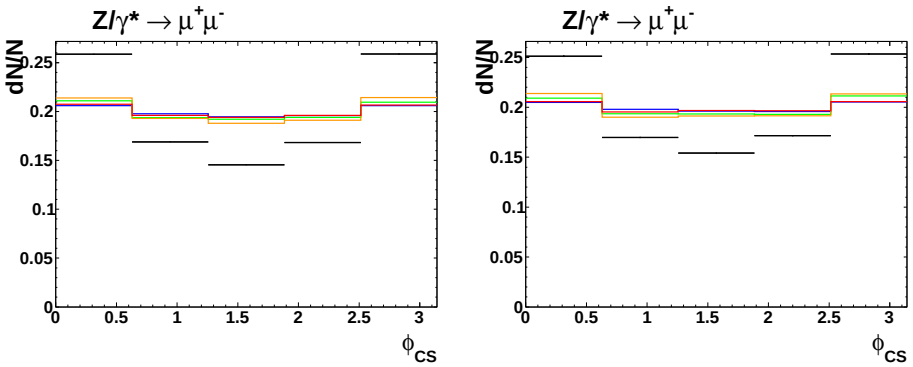

(a) $1 < p_T^{ll} < 15$ GeV/c

(b) $15 < p_T^{ll} < 30$ GeV/c

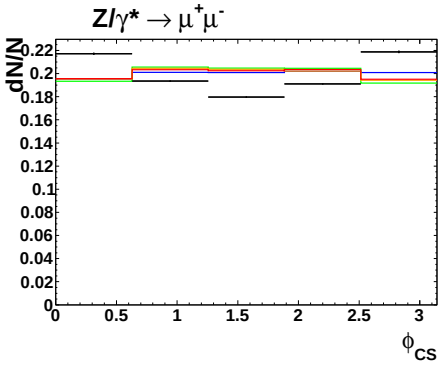

(c) $30 < p_T^{ll} < 40$ GeV/c

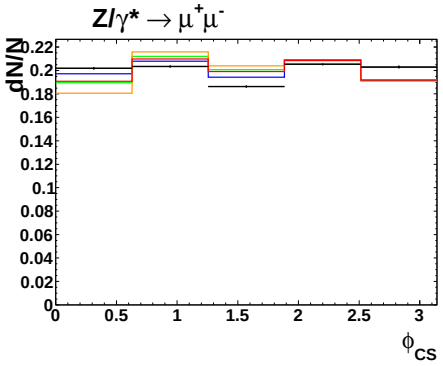

(d) $40 < p_T^{ll} < 50$ GeV/c

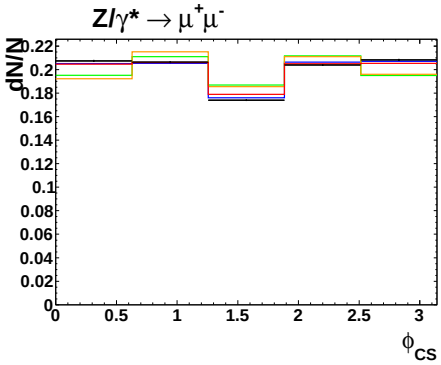

(e) $50 < p_T^{ll} < 100$ GeV/c

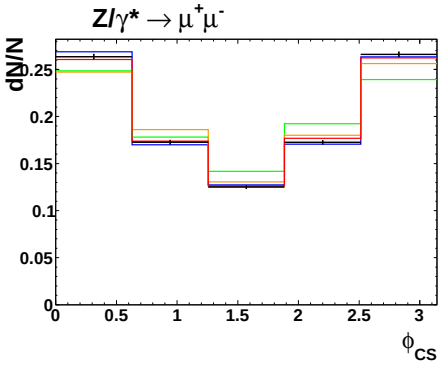

(f) $100 < p_T^{ll} < 180$ GeV/c

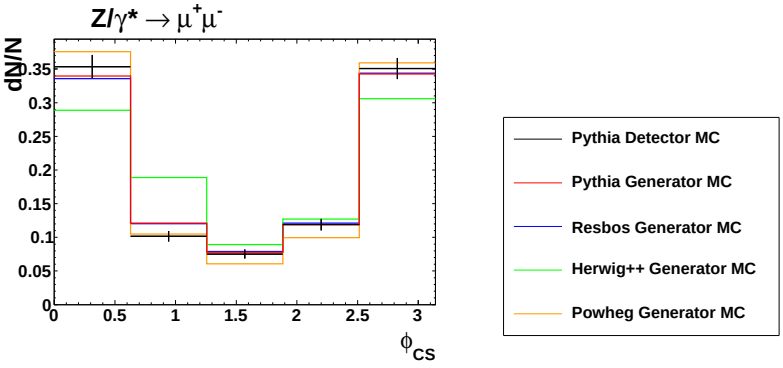

(g) $p_T^{ll} > 180$ GeV/c

Figure 4.12: ϕ_{CS} distributions for dimuon PYTHIA, RESBOS, POWHEG and HERWIG++ generator MC samples compared to PYTHIA detector MC.

Chapter 5

Backgrounds

5.1 Sources of Experimental Backgrounds

The main dielectron and dimuon backgrounds are from $Z \rightarrow \tau\tau$, $t\bar{t}$ and WW diboson production. These processes all contain two oppositely charged leptons in the final state (according to the Standard Model) and can pass the selection requirements for this analysis. Detector level MC samples are produced for each of these backgrounds.

Figures 5.1a to 5.1c show the Feynman diagram representations of the main shared dielectron and dimuon background processes.

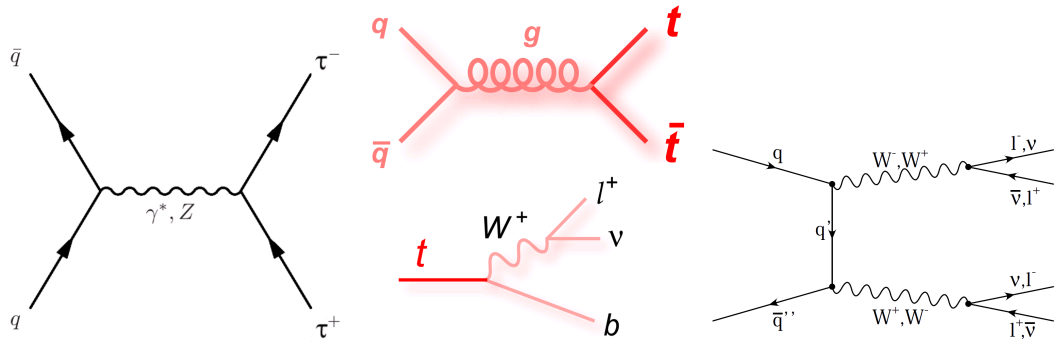

(a) $Z \rightarrow \tau\tau$ (b) $t\bar{t}$ (c) $W^+ + W^- \rightarrow l^+l^-\nu\bar{\nu}$

Figure 5.1: Feynman diagrams for the main dilepton SM backgrounds for this analysis.

5.1.1 $Z \to \tau\tau$ Production

$Z \to \tau\tau$ is the dominant background source of the three main shared backgrounds, the $\tau^+\tau^-$ pair can be created in the same way as $Z/\gamma^* \to e^+e^-$ and $Z/\gamma^* \to \mu^+\mu^-$ production, as shown if figure 5.1a, with the τ^+ (τ^-) then decaying to an electron/muon (positron/antimuon) plus two neutrinos. The detector measures only two leptons in the final state as neutrinos pass through the detector unobserved, giving the event an identical final state signature to the signal process. However, as the τ has an invariant mass of 1.78 GeV/c^2 there is not much available phase space left from the Z/γ^* decay so the p_Ts of the τ decay products are low and can mostly be removed by the selection requirement on individual lepton p_Ts.

5.1.2 $t\bar{t}$ and WW Production

Production of $t\bar{t}$ pairs decaying to $t\bar{t} \to l^+l^-\nu\bar{\nu}b\bar{b}$ final states and WW diboson production decaying to $W^+ + W^- \to l^+l^-\nu\bar{\nu}$ final states are legitimate backgrounds to the dielectron and dimuon Drell-Yan process in the sense that the decays of these systems can contain two oppositely charged leptons in the final state, however the production cross section for these processes are much lower than for the dielectron and dimuon signal processes.

5.1.3 Cosmic Ray Muons

An important additional background to the dimuon analysis comes from cosmic ray muons, where a single cosmic ray muon passing through the detector can produce a detector signal analogous to dimuon signal final state. As the $\mu^{\cos}$ originates outside the detector it effectively passes through one half of the detector "backwards" (passing first through the muon system then through the EM calorimeter and the central

tracking system). It then passes through the other half of the detector in the usual fashion for muons produced at the interaction point of the proton-antiproton beams. As the muon (antimuon) passes backwards through the detector, the curved path of its trajectory is similar to the track that would be made by an equivalent antimuon (muon) moving in the opposite direction, away from the interaction point. This leads to the detector recording the event as two back-to-back oppositely charged muons, however certain properties of the $\mu^{\cos}$system are much different to the dimuon signal events.

As explained in chapter 3 selection cuts to remove cosmic ray muons are applied to muon system timing information, DCA and colinearity of tracks. $\mu^{\cos}$s have a larger time difference between the two instances when they pass through the muon detection system compared to signal events as the $\mu^{\cos}$has to travel across the width of the detector inbetween passing through the muon system twice. $\mu^{\cos}$s also rarely pass close to the centre of the detector which the cut on DCA accounts for. Finally, $\mu^{\cos}$ tracks are collinear, as it is the same e particle being measured for both tracks, so introducing a selection cut omitting events with very collinear tracks combined with the other $\mu^{\cos}$ cuts removes almost all $\mu^{\cos}$ events while maintaining the vast majority of signal events.

5.2 Background Plots

Plots in this section show the distributions, at detector level, of combined signal and backgrounds MC compared to data for different variables. With the vertical axis showing the number of events in each bin, N_E.

Figures 5.2a to 5.2d show the stacked signal plus background ($Z \rightarrow \tau\tau$, $t\bar{t}$ and WW) MC compared to data for the distributions of positive and negative lepton p_Ts for dielectron and dimuon samples after all selection cuts. These plots show

good agreement between data and MC as well as a large dominance of signal MC over combined backgrounds. From this it is possible to treat the analysis as a signal dominated process and it is possible to neglect SM backgrounds as a major source of uncertainty.

Figures 5.3a to 5.5d show the stacked signal plus background distributions compared to data for p_T^{ll}, M_{inv}^{ll}, η_{det} and dilepton y. The p_T^{ll} and M_{inv}^{ll} distributions all show good agreement between data and MC except for figure 5.3c which shows a slight excess of MC over data at high p_T^{ll}. However, statistics over this range are quite low.

The η_{det} and dilepton y distributions show poor agreement between data and MC in the dimuon channel, this is due to the track χ^2 requirement made for the dimuon analysis which illuminates the poor η modelling of the muon detector simulation. The dielectron channel shows a slight excess of MC over data in the η_{det} distribution for $|\eta_{\text{det}}| > 2$ due to the overestimation of the measurement efficiency in this region for the electron detector simulation. sytematic uncertainties due to this mismodelling are estimated in chapter 6.1.

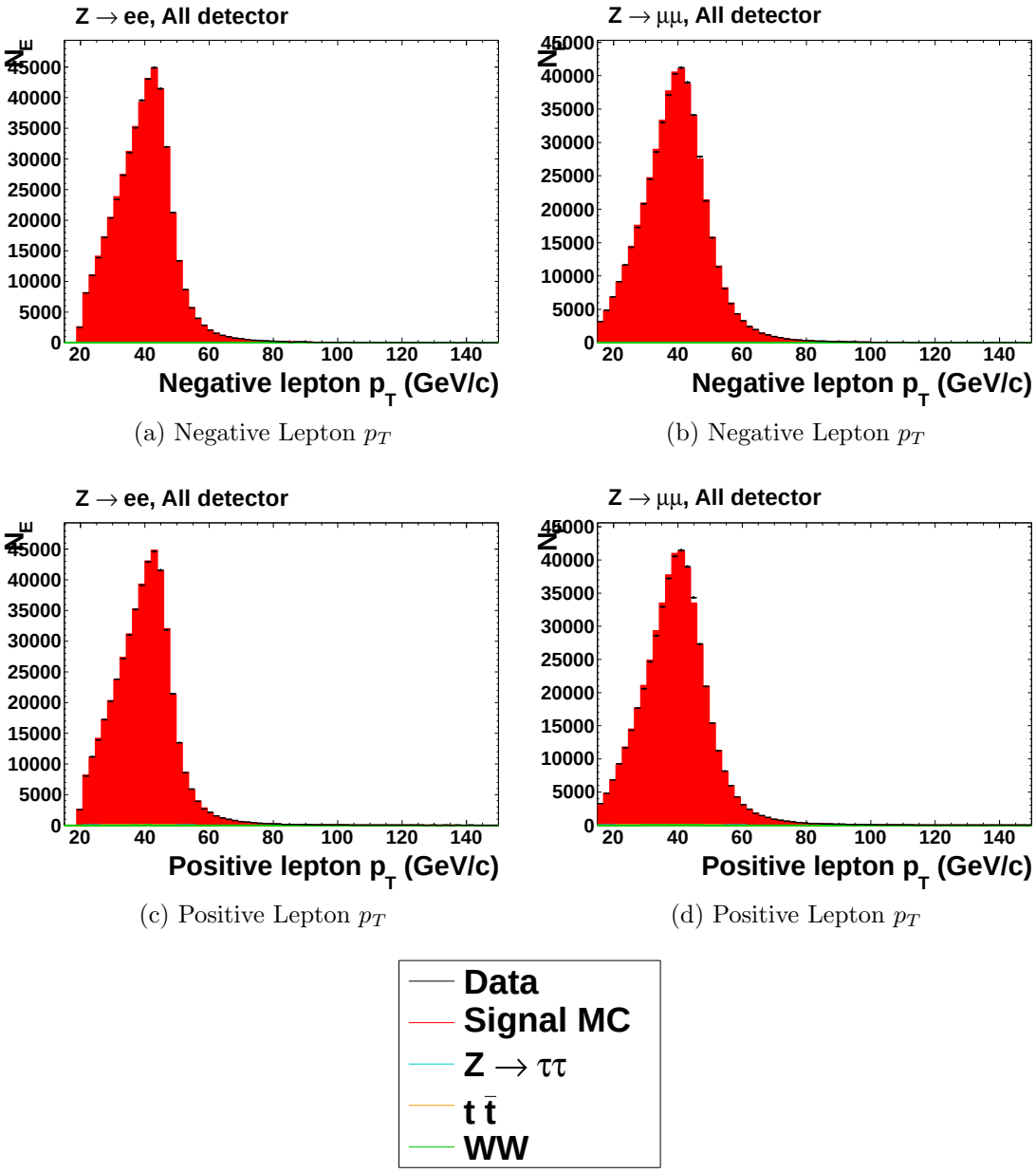

(a) Negative Lepton p_T

(b) Negative Lepton p_T

(c) Positive Lepton p_T

(d) Positive Lepton p_T

Figure 5.2: Stacked signal plus backgrounds MC p_T distributions for individual positive and negative leptons compared to data for dielectron and dimuon analyses.

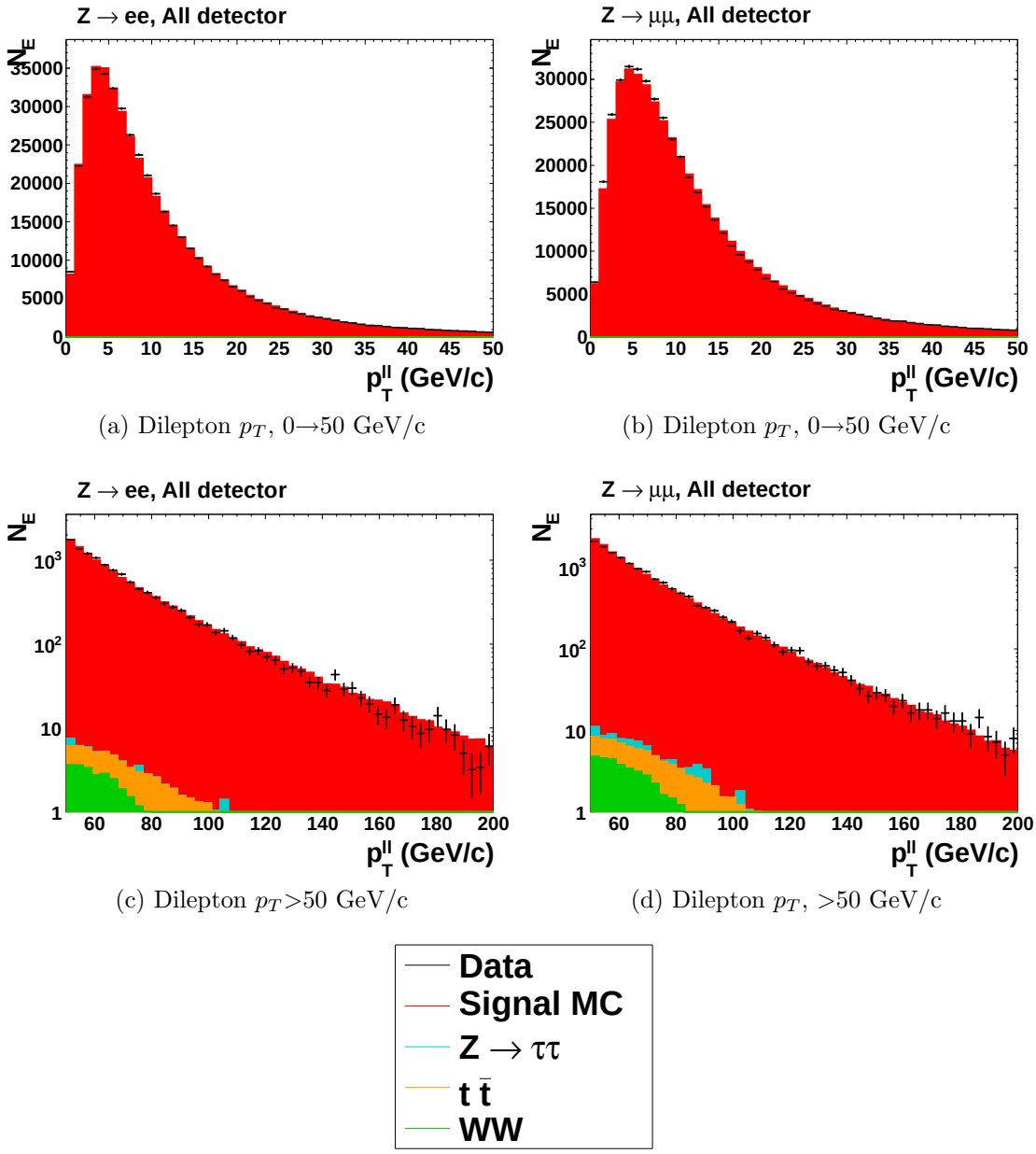

(a) Dilepton p_T, 0→50 GeV/c

(b) Dilepton p_T, 0→50 GeV/c

(c) Dilepton p_T>50 GeV/c

(d) Dilepton p_T, >50 GeV/c

Figure 5.3: Stacked signal plus backgrounds MC p_T^{ll} distributions compared to data for dielectron and dimuon analyses. p_T^{ll} plotted over the range $0 < p_T^{ll} < 50$ GeV/c with linear scale vertical axis, and over the range $50 < p_T^{ll} < 200$ with a logarithmic scale vertical axis.

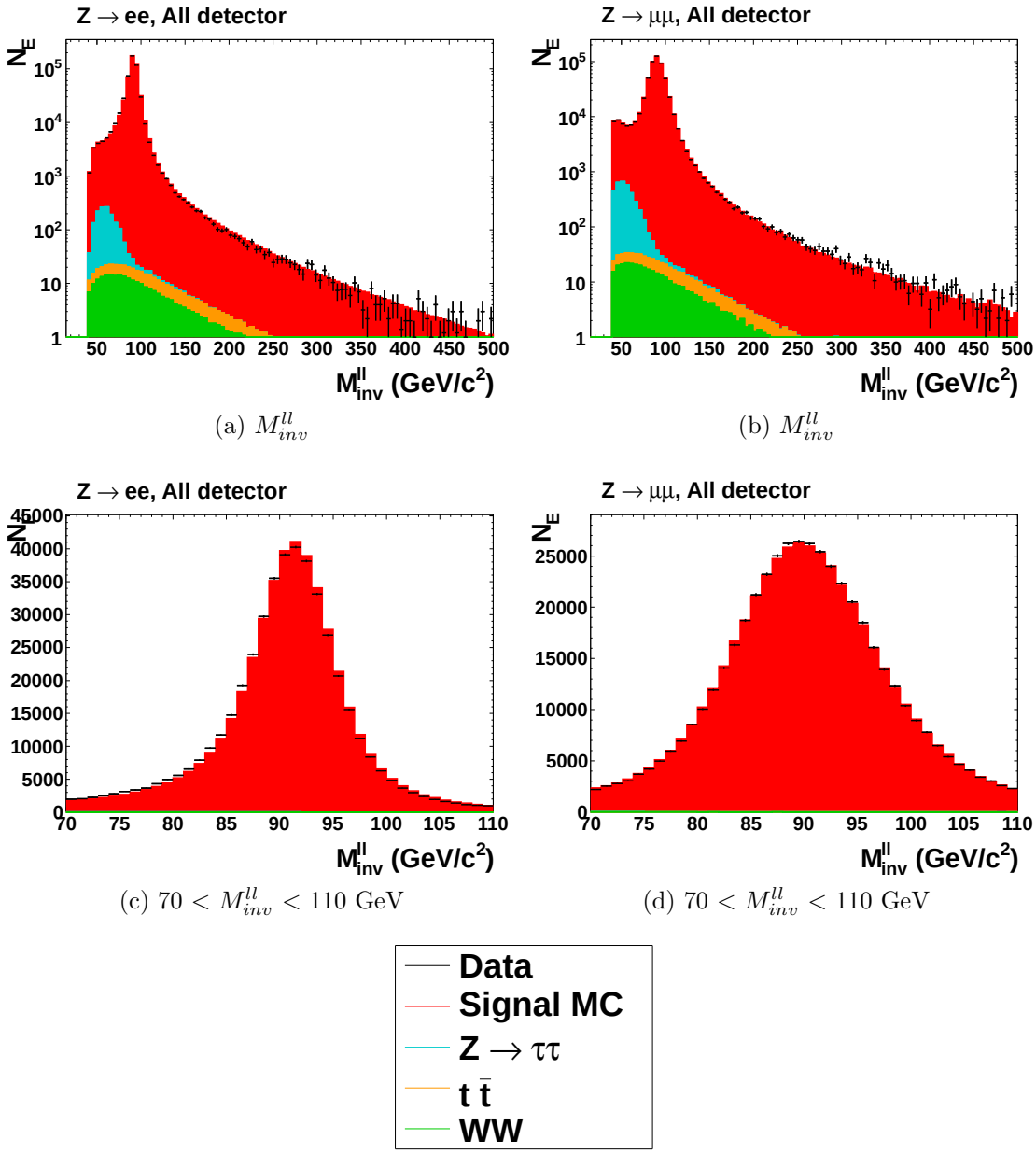

(a) M_{inv}^{ll} (b) M_{inv}^{ll}

(c) $70 < M_{inv}^{ll} < 110$ GeV (d) $70 < M_{inv}^{ll} < 110$ GeV

Figure 5.4: Stacked signal plus backgrounds M_{inv}^{ll} distributions compared to data for dielectron and dimuon analyses. M_{inv}^{ll} plotted over the range $30 < M_{inv}^{ll} < 500$ GeV/c^2 with logarithmic scale vertical axis, and over the range $70 < M_{inv}^{ll} < 110$ GeV/c^2.

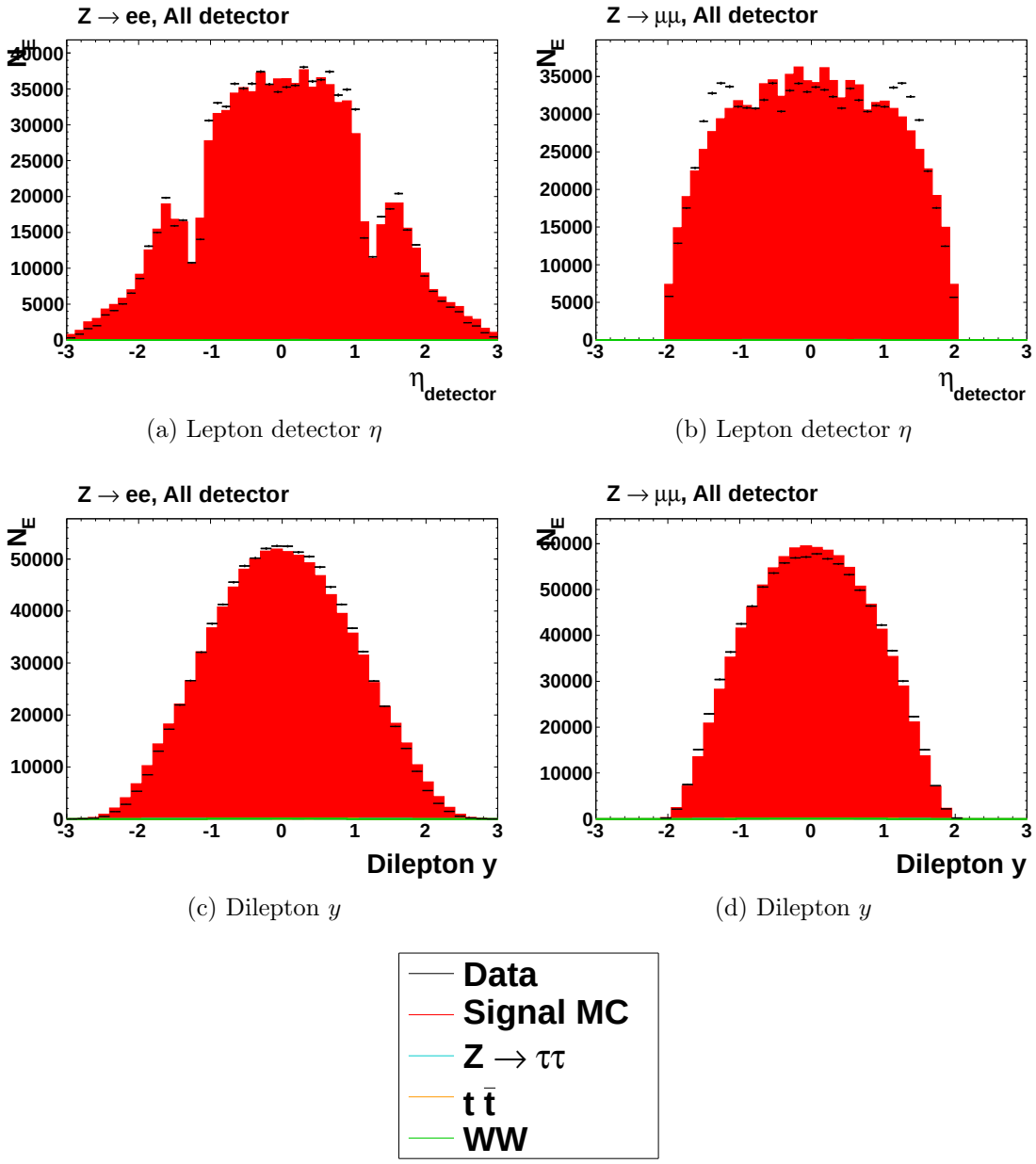

(a) Lepton detector η

(b) Lepton detector η

(c) Dilepton y

(d) Dilepton y

Figure 5.5: Stacked signal plus backgrounds MC η_{det} and dilepton y distributions compared to data for dielectron and dimuon analyses.

The PYTHIA detector level MC samples do not contain any simulation of cosmic ray muons, therefore it is important that the event selection cuts are effective at removing cosmic ray muons from the data samples.

Figures 5.6a and 5.6b show distributions of $\eta_1 + \eta_2$ before and after the specific cuts on $\mu^{\cos}$s are applied. As expected, figure 5.6a shows a sharply peaked excess over the combined MC signal and background samples in the data distribution around $\eta_1 + \eta_2 = 0$ corresponding to the cosmic ray muons, which pass all other selection cuts, existent in the dimuon data sample. Figure 5.6b shows the same distribution with the cut on $\mu^{\cos}$ applied showing no visible sign of any cosmic ray muon events and with good agreement between data and MC across the distribution.

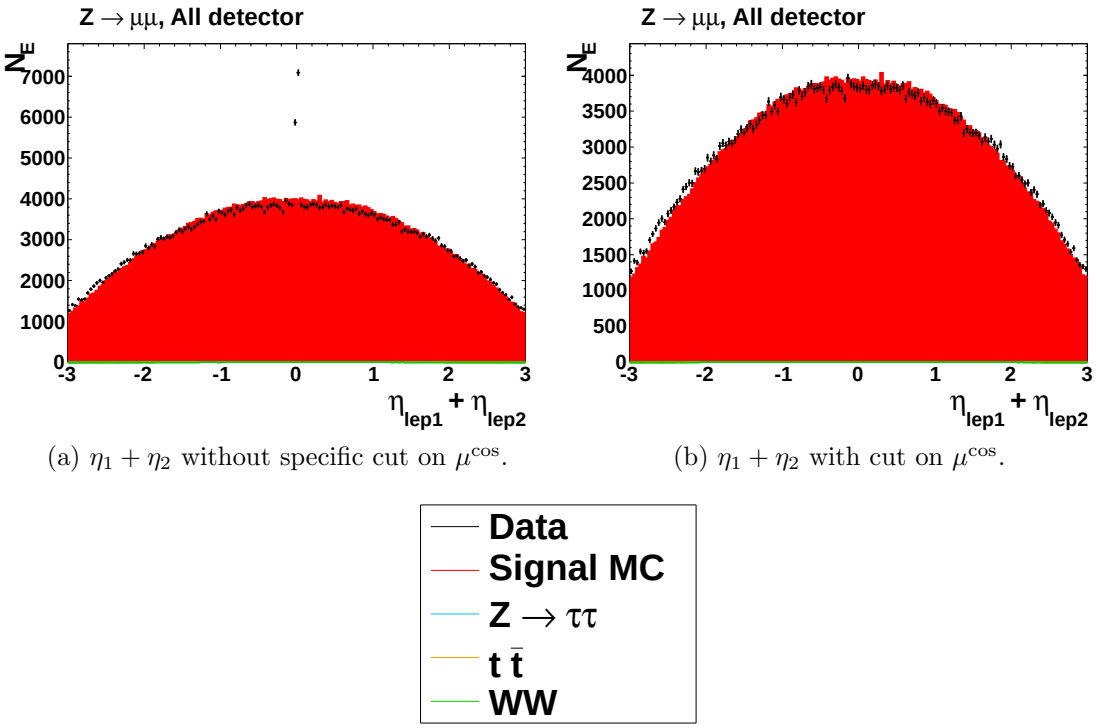

(a) $\eta_1 + \eta_2$ without specific cut on $\mu^{\cos}$.

(b) $\eta_1 + \eta_2$ with cut on $\mu^{\cos}$.

Figure 5.6: Stacked signal plus backgrounds MC $\eta_1+\eta_2$ distributions with and without cosmic ray selection cuts compared to data.

Figures 5.7a to 5.8g show the combined signal plus backgrounds $\phi_{\rm CS}$ distributions compared to data. These plots show good agreement between data and MC in the region of $p_T^{ll}<$ 100 GeV/c, within statistical uncertainties.

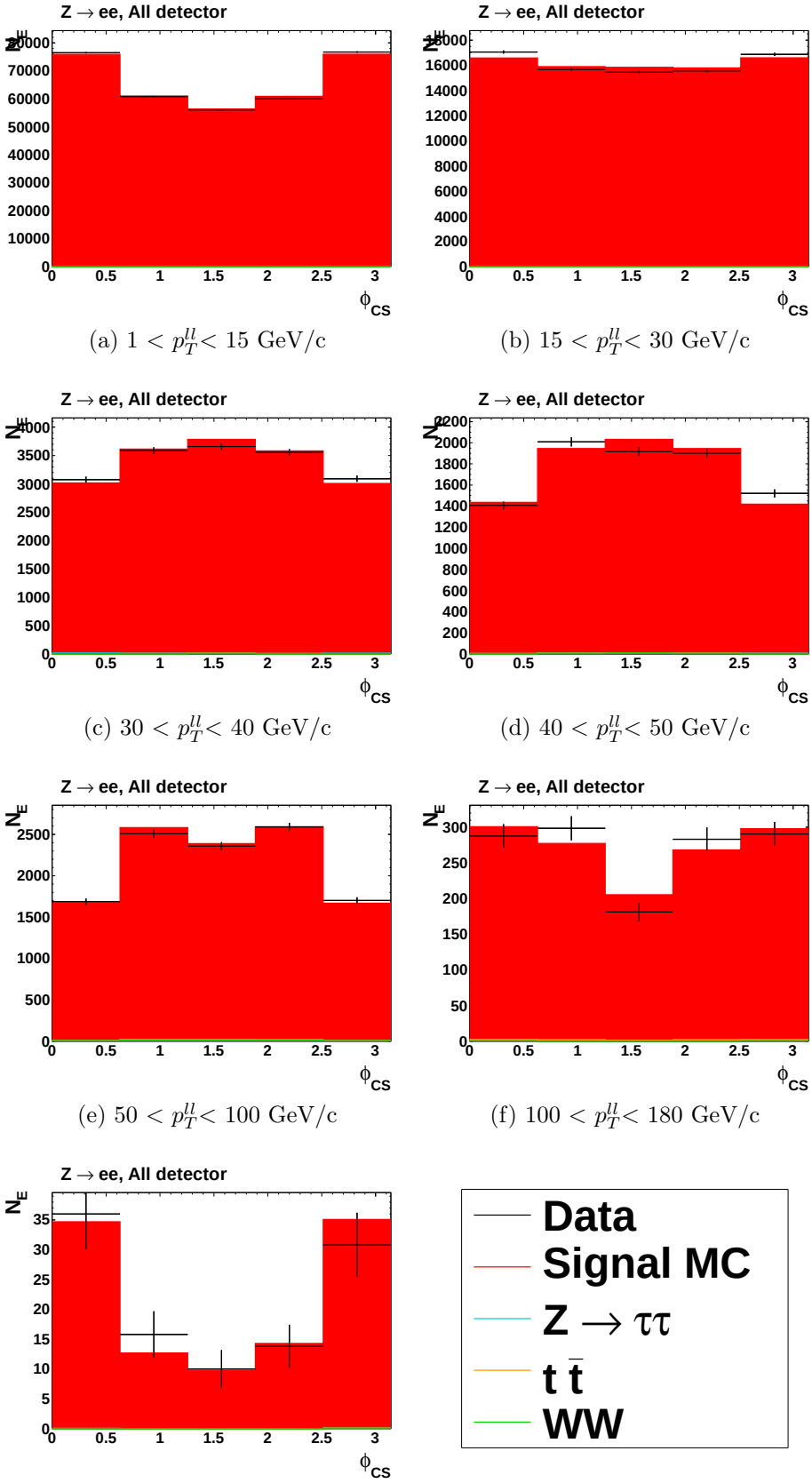

(a) $1 < p_T^{ll} < 15$ GeV/c

(b) $15 < p_T^{ll} < 30$ GeV/c

(c) $30 < p_T^{ll} < 40$ GeV/c

(d) $40 < p_T^{ll} < 50$ GeV/c

(e) $50 < p_T^{ll} < 100$ GeV/c

(f) $100 < p_T^{ll} < 180$ GeV/c

(g) $p_T^{ll} > 180$ GeV/c

Figure 5.7: $\phi_{\rm CS}$ distributions for dielectron signal MC and SM backgrounds compared to data.

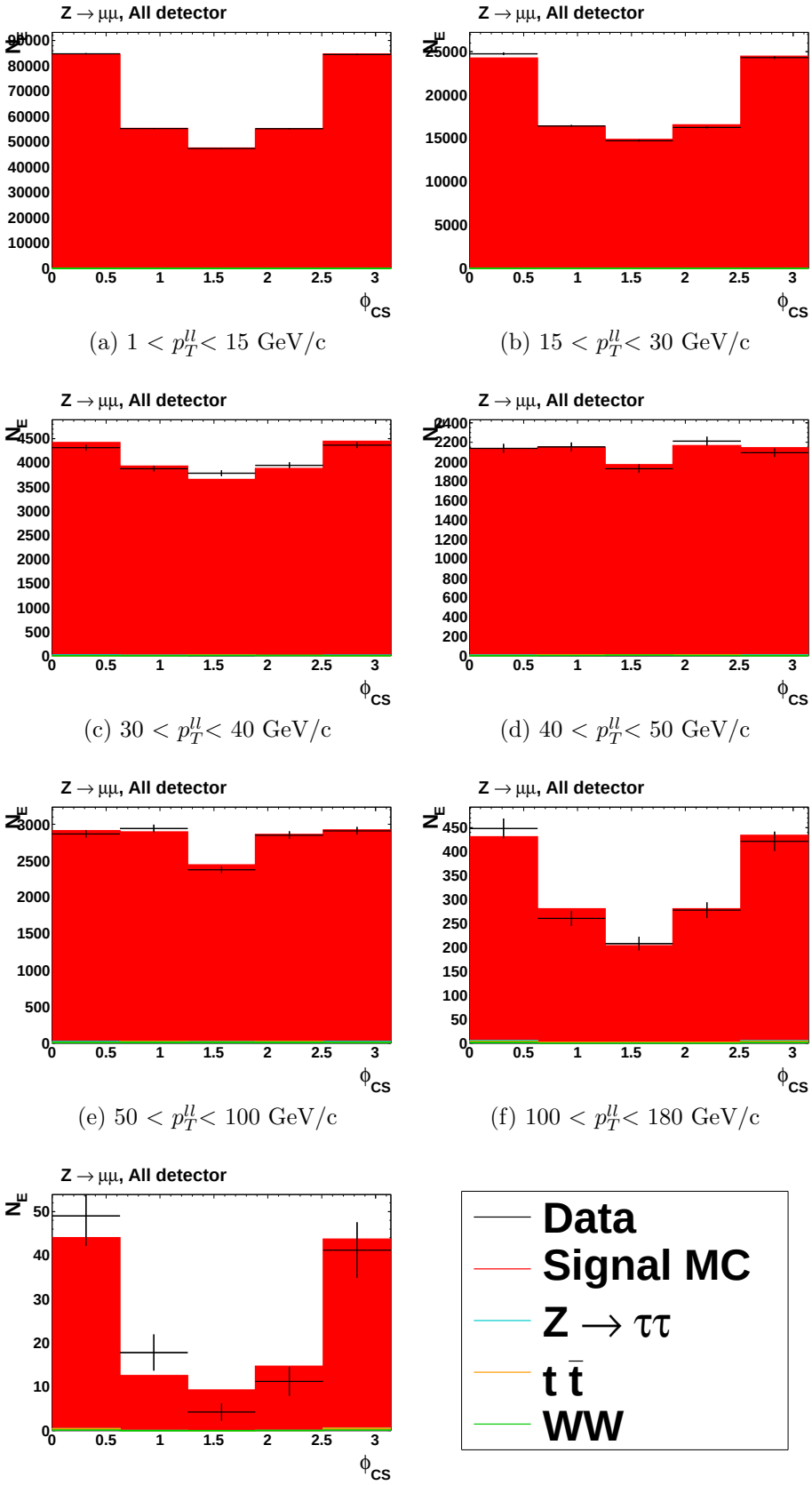

(a) $1 < p_T^{ll} < 15$ GeV/c

(b) $15 < p_T^{ll} < 30$ GeV/c

(c) $30 < p_T^{ll} < 40$ GeV/c

(d) $40 < p_T^{ll} < 50$ GeV/c

(e) $50 < p_T^{ll} < 100$ GeV/c

(f) $100 < p_T^{ll} < 180$ GeV/c

(g) $p_T^{ll} > 180$ GeV/c

Figure 5.8: $\phi_{\rm CS}$ distributions for dimuon signal MC and SM backgrounds compared to data.

Chapter 6

Corrections to Data

6.1 Bin by Bin Correction Factors

To enable a comparison between data and generator level MC ϕ_{CS} distributions bin-by-bin correction factors are calculated for each ϕ_{CS} distribution. These correction factors are calculated by dividing each PYTHIA generator MC ϕ_{CS} distribution by the corresponding PYTHIA detector MC distribution for each p_T range that ϕ_{CS} is measured over. The ϕ_{CS} distributions for the data are then multiplied by these correction factor histograms to give the final data distributions which can be compared to generator MC samples.

Figures 6.1a to 6.1g and 6.2a to 6.2g show generator level and detector level MC ϕ_{CS} distributions with their corresponding correction factors for dielectron and dimuon samples.

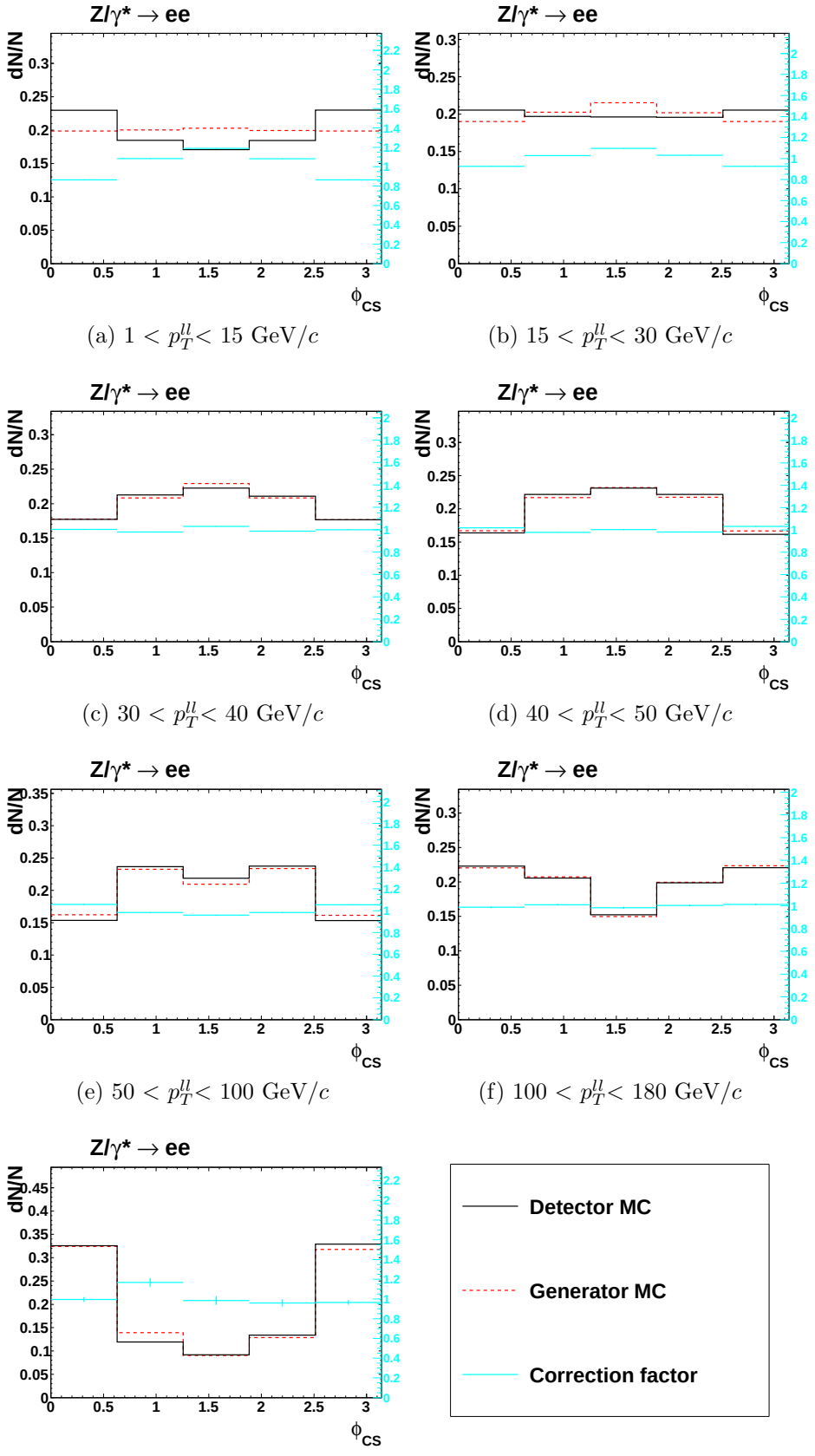

(a) $1 < p_T^{ll} < 15$ GeV/c

(b) $15 < p_T^{ll} < 30$ GeV/c

(c) $30 < p_T^{ll} < 40$ GeV/c

(d) $40 < p_T^{ll} < 50$ GeV/c

(e) $50 < p_T^{ll} < 100$ GeV/c

(f) $100 < p_T^{ll} < 180$ GeV/c

(g) $p_T^{ll} > 180$ GeV/c

Figure 6.1: Dielectron ϕ_{CS} distributions for nominal generator and detector level Monte Carlo with associated correction factor.

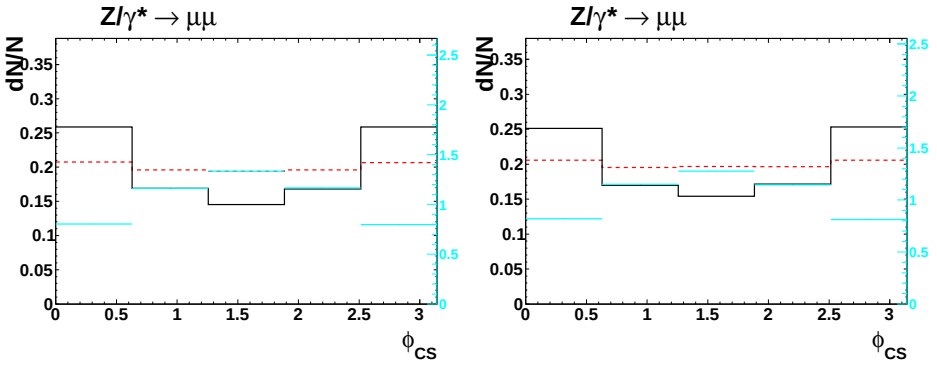

(a) $1 < p_T^{ll} < 15$ GeV/c

(b) $15 < p_T^{ll} < 30$ GeV/c

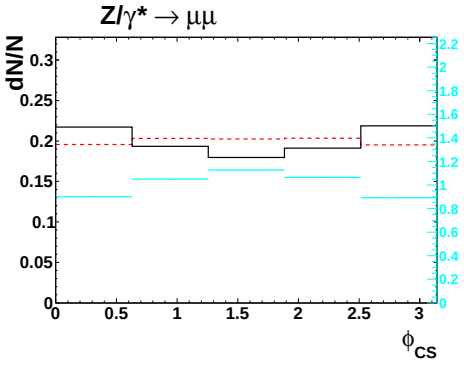

(c) $30 < p_T^{ll} < 40$ GeV/c

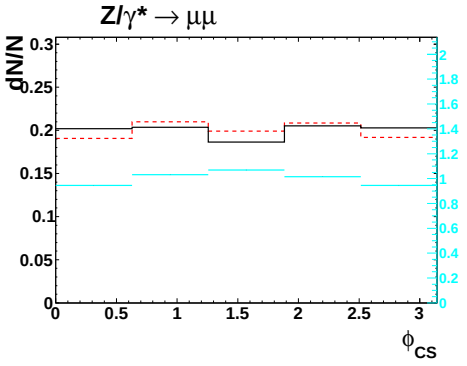

(d) $40 < p_T^{ll} < 50$ GeV/c

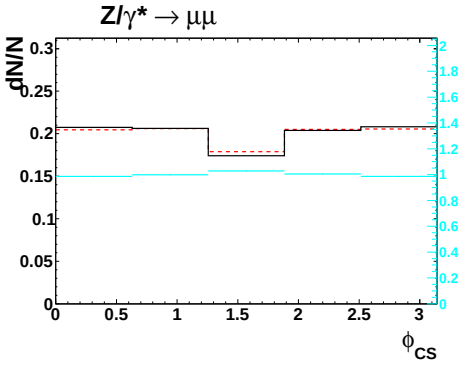

(e) $50 < p_T^{ll} < 100$ GeV/c

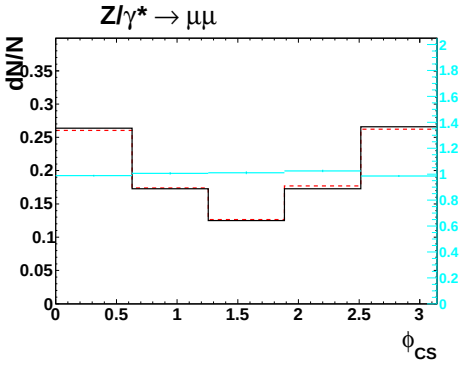

(f) $100 < p_T^{ll} < 180$ GeV/c

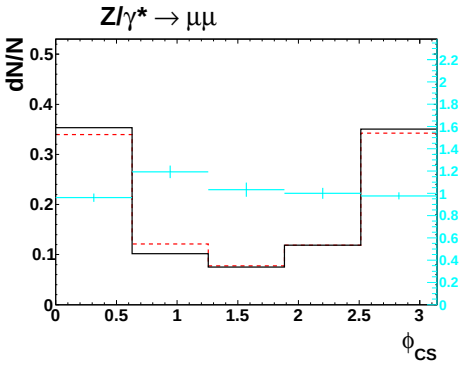

(g) $p_T^{ll} > 180$ GeV/c

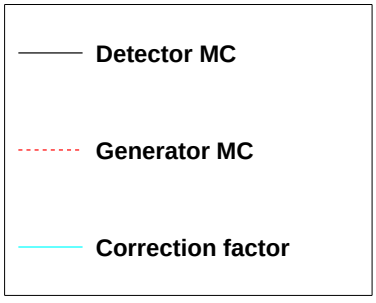

Figure 6.2: Dimuon $\phi_{\rm CS}$ distributions for nominal generator and detector level Monte Carlo with associated correction factor.

6.2 Systematic Uncertainties

To estimate the systematic uncertainties on the ϕ_{CS} distributions various smearings and reweightings are applied to MC samples and their effects on the measured correction factor are determined. The applied smearings and reweightings are as such:

- p_T smearing. Gaussian smearing in range $\pm 1.5\%$ applied to detector MC lepton p_T. This smearing is applied to test the sensitivity of the ϕ_{CS} distribution to the p_T resolution of the detector.

- p_T scale. All detector MC events have lepton p_T weighted down by 0.04%.

- η reweighting. Detector MC lepdeteta distribution weighted down by 20% in the region $|\eta|>1.1$ to testϕ_{CS} measurement sensitivity to events with leptons outside the CC region.

- Resbos Z p_T and rapidity reweighting change. Events for Resbos Z p_T reweighted samples reweighted at generator and detector level such that:

$$w = w_R + 0.5 \times |w_R - w_0| \tag{6.1}$$

  where w is the final event weight, w_0 is the event weight without Resbos reweighting applied and w_R is the event weight after Resbos reweighting.

- ϕ_{CS} reweighting. ϕ_{CS} distributions weighted up by a factor of 1.05 in the range $\frac{\pi}{4} < \phi_{\text{CS}} < \frac{3\pi}{4}$ at both generator and detector level in MC. This reweighting is used to test how the calculated correction factor needed to apply to the data is changed by a shift in the expected ϕ_{CS} distribution in the MC simulation.

6.3 Smearings and Reweightings Compared to Data

The plots in this section show the effects of the systematic reweightings and smearings on various distributions and their affects on the measured ϕ_{CS} correction factor.

Figures 6.3a to 6.3d show the M_{inv}^{ll} distributions for nominal MC, p_T smear and p_T scale samples compared to data for dielectron and dimuon analysis along with the corresponding plots showing data/MC for each sample.

Figures 6.4a and 6.4b show the dielectron and dimuon η_{det} distributions for the nominal MC and $|\eta_{\text{det}}|$ reweighting samples compared to data. This reweighting appears to span the difference between data and nominal MC for the dielectron sample however in the dimuon sample the shapes of the data and MC distributions are so different that it is less clear if this reweighting covers the entire range of the systematic uncertainty caused by the difference in shape between data and nominal MC.

Figures 6.5a to 6.5d show the p_T^{ll} distributions for nominal MC and modified RESBOS reweighting samples compared to data for dielectron and dimuon analysis.

Figures 6.6a to 6.7g show the ϕ_{CS} distributions for nominal MC and reweighted ϕ_{CS}samples compared to data for dielectron and dimuon analysis. The reweighting appears to span more than the difference between data and MC at low p_T^{ll} but doesn't span the difference at high p_T^{ll} where statistical uncertainties are large.

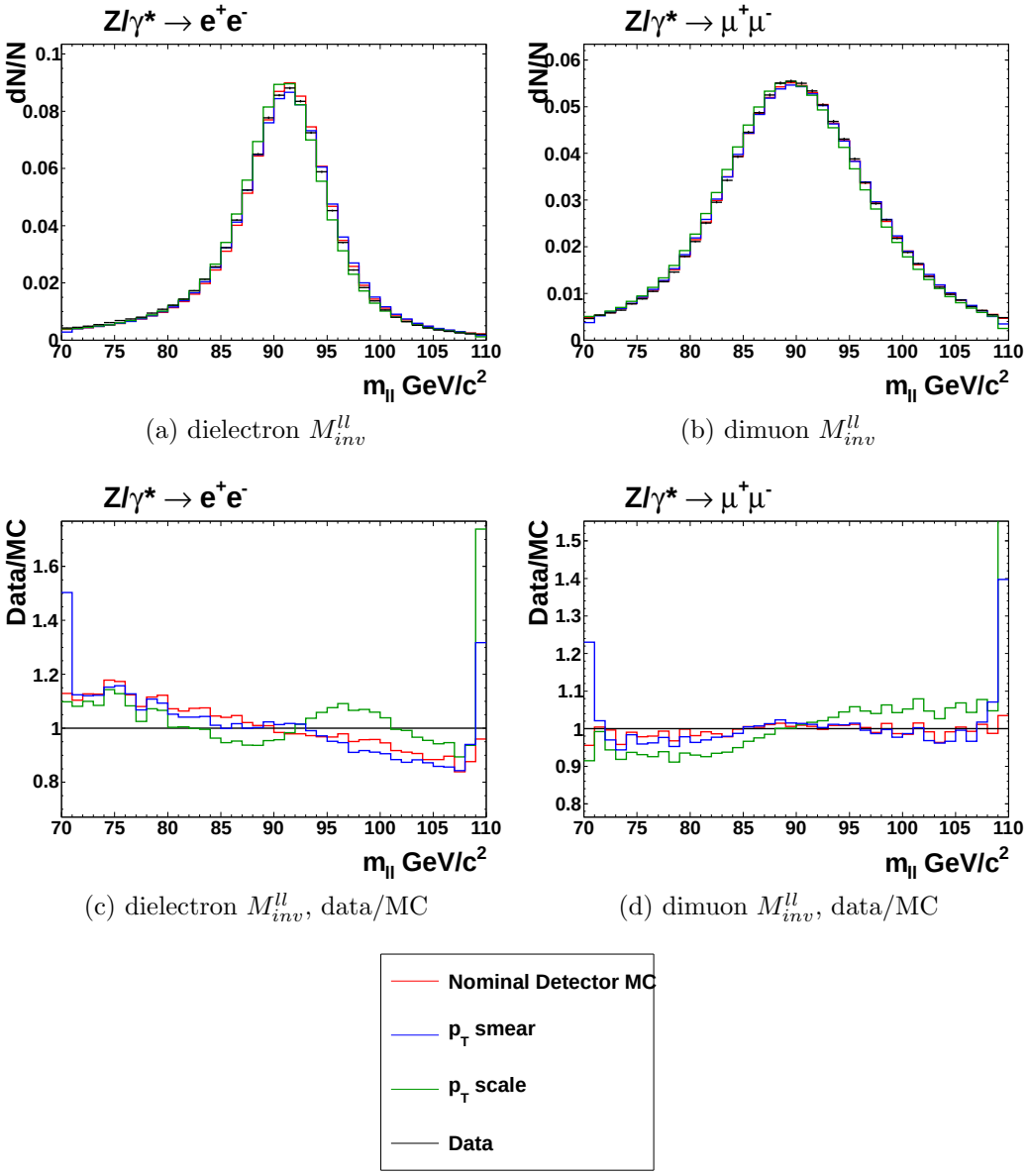

(a) dielectron M_{inv}^{ll}

(b) dimuon M_{inv}^{ll}

(c) dielectron M_{inv}^{ll}, data/MC

(d) dimuon M_{inv}^{ll}, data/MC

Figure 6.3: M_{inv}^{ll} distributions and the ratio of data to MC for nominal detector MC, p_T smear and p_T scale dielectron and dimuon samples.

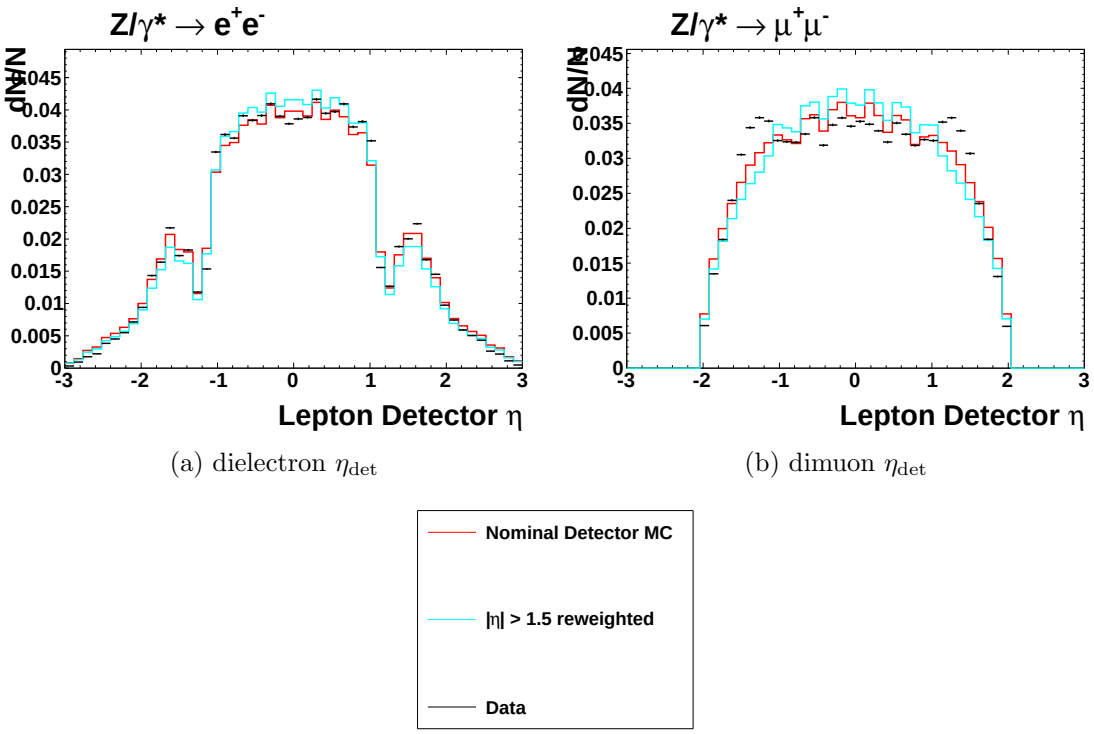

(a) dielectron η_{det}

(b) dimuon η_{det}

Figure 6.4: Detector η distributions for dielectron and dimuon nominal and η efficiency detector MC samples, compared to data

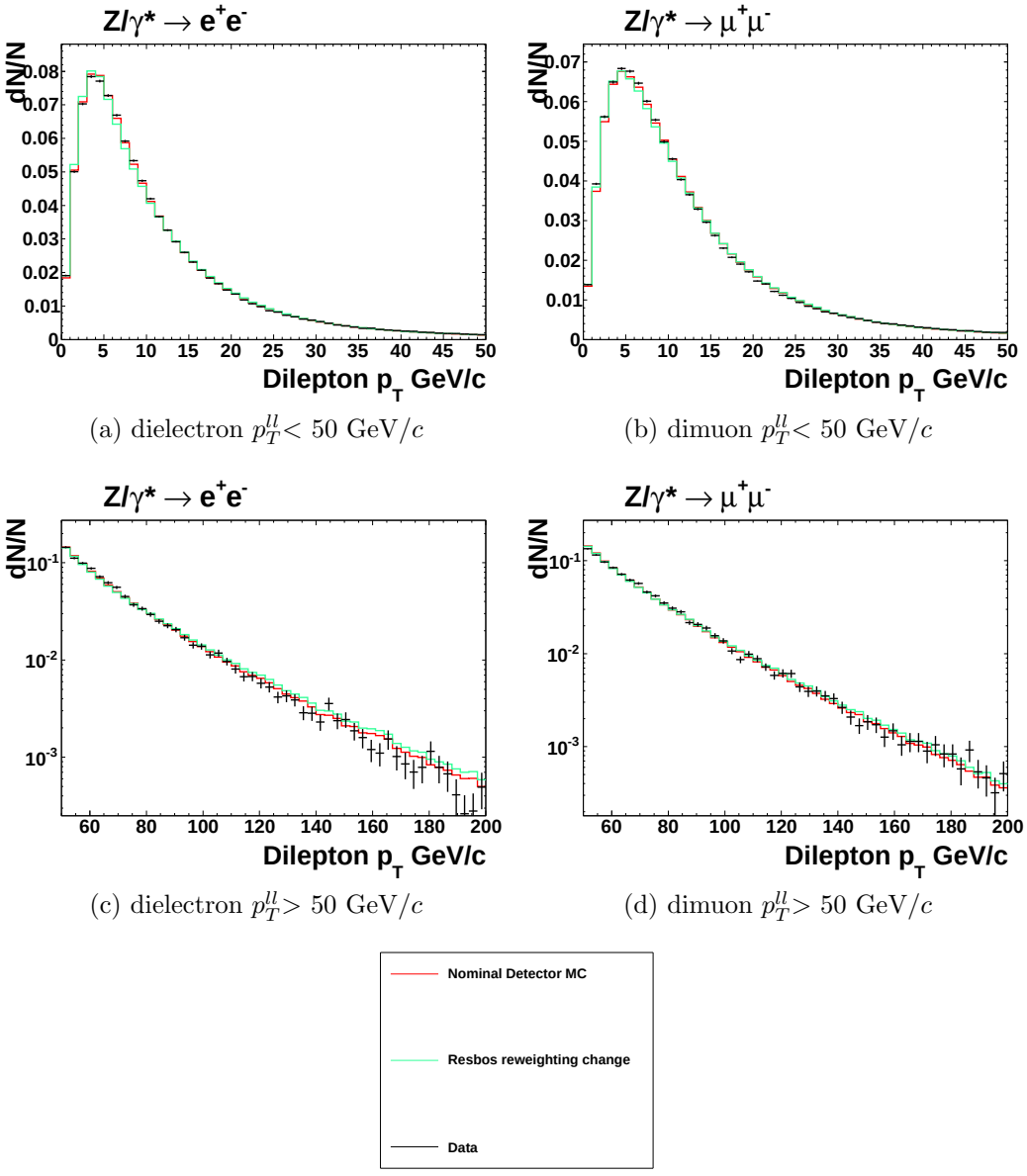

(a) dielectron $p_T^{ll} < 50$ GeV/c

(b) dimuon $p_T^{ll} < 50$ GeV/c

(c) dielectron $p_T^{ll} > 50$ GeV/c

(d) dimuon $p_T^{ll} > 50$ GeV/c

Figure 6.5: p_T^{ll} distributions for nominal detector MC and modified RESBOS reweighting samples compared to data for dielectron and dimuon events.

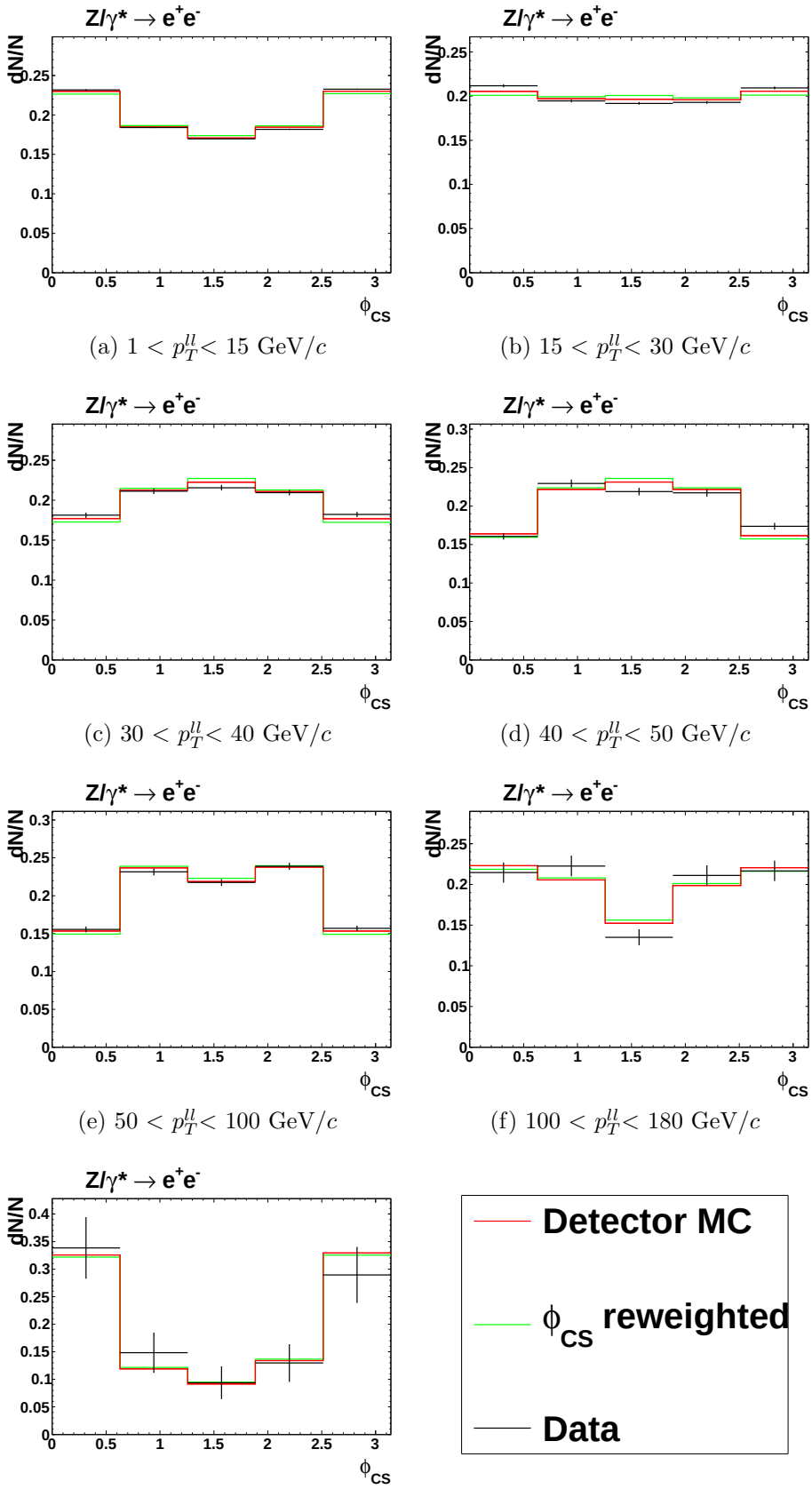

(a) $1 < p_T^{ll} < 15$ GeV/c

(b) $15 < p_T^{ll} < 30$ GeV/c

(c) $30 < p_T^{ll} < 40$ GeV/c

(d) $40 < p_T^{ll} < 50$ GeV/c

(e) $50 < p_T^{ll} < 100$ GeV/c

(f) $100 < p_T^{ll} < 180$ GeV/c

(g) $p_T^{ll} > 180$ GeV/c

Figure 6.6: Dielectron ϕ_{CS} distributions for nominal detector MC and ϕ_{CS} reweighted samples compared to data.

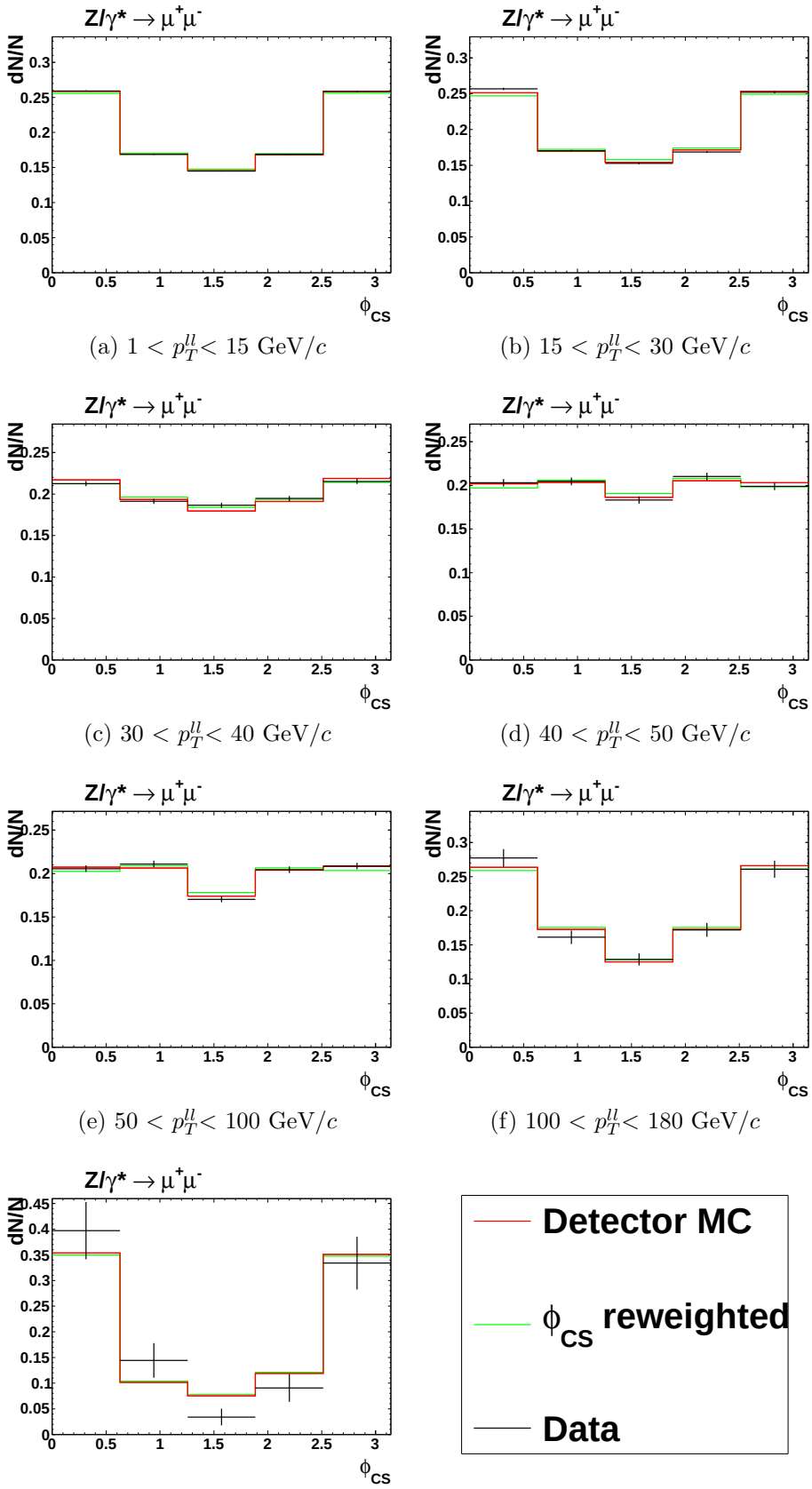

(a) $1 < p_T^{ll} < 15$ GeV/c

(b) $15 < p_T^{ll} < 30$ GeV/c

(c) $30 < p_T^{ll} < 40$ GeV/c

(d) $40 < p_T^{ll} < 50$ GeV/c

(e) $50 < p_T^{ll} < 100$ GeV/c

(f) $100 < p_T^{ll} < 180$ GeV/c

(g) $p_T^{ll} > 180$ GeV/c

Figure 6.7: Dimuon ϕ_{CS} distributions for nominal detector MC and ϕ_{CS} reweighted samples compared to data.

Figures 6.8a to 6.8g and figures 6.9a to 6.9g show plots of λ for each systematic smearing/reweighting, where λ is defined as

$$\lambda = \frac{|\mathrm{cf}^{'} - \mathrm{cf}_{nom}|}{\mathrm{cf}_{nom}} \tag{6.2}$$

where $\mathrm{cf}^{'}$ is the modified correction factor and cf_{nom} is the nominal correction factor.

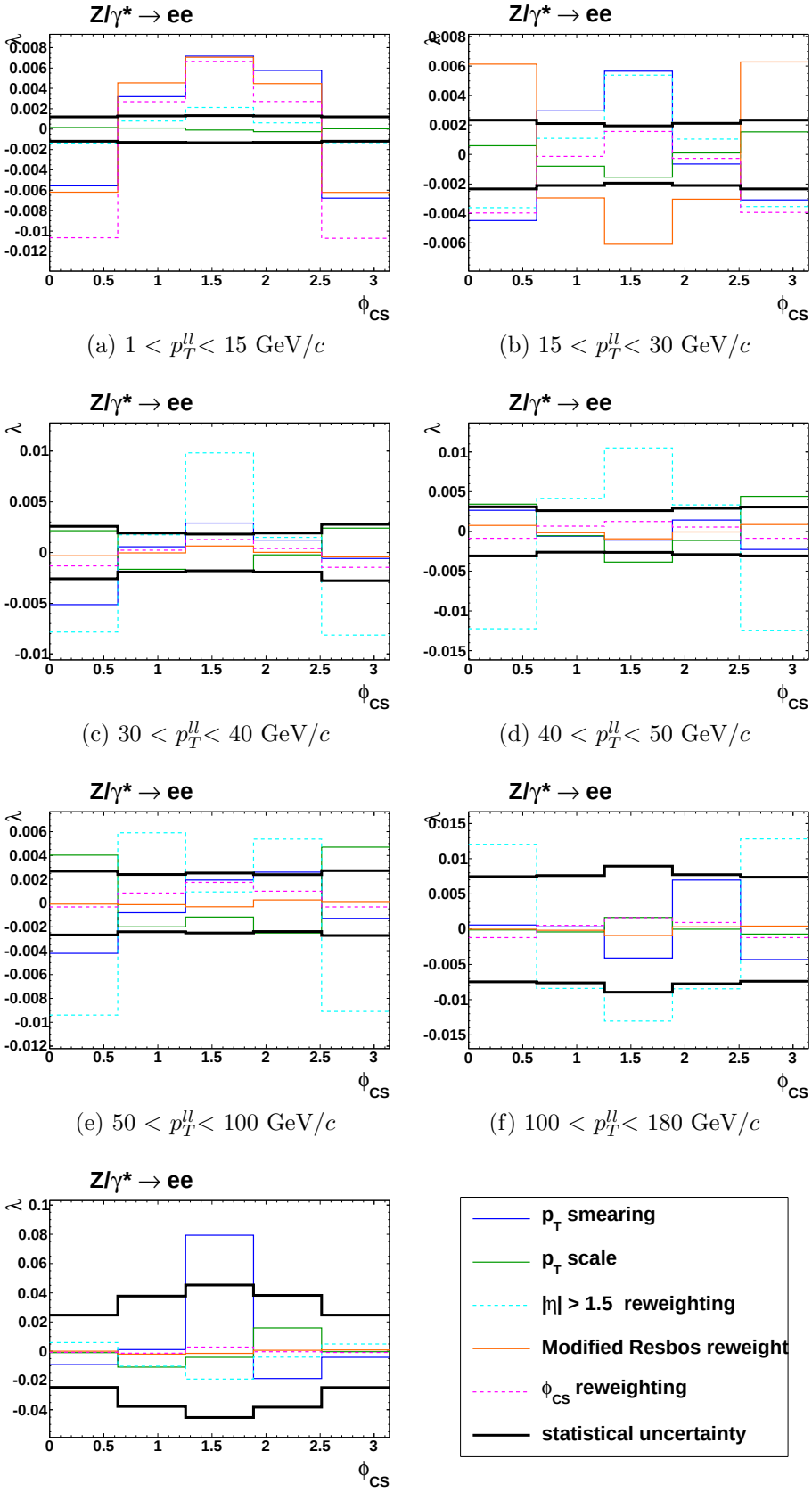

(a) $1 < p_T^{ll} < 15$ GeV/c

(b) $15 < p_T^{ll} < 30$ GeV/c

(c) $30 < p_T^{ll} < 40$ GeV/c

(d) $40 < p_T^{ll} < 50$ GeV/c

(e) $50 < p_T^{ll} < 100$ GeV/c

(f) $100 < p_T^{ll} < 180$ GeV/c

(g) $p_T^{ll} > 180$ GeV/c

Figure 6.8: Ratio of |smeared or reweighted correction factor - nominal correction factor| to nominal correction factor for dielectron detector MC $\phi_{\rm CS}$ sample.

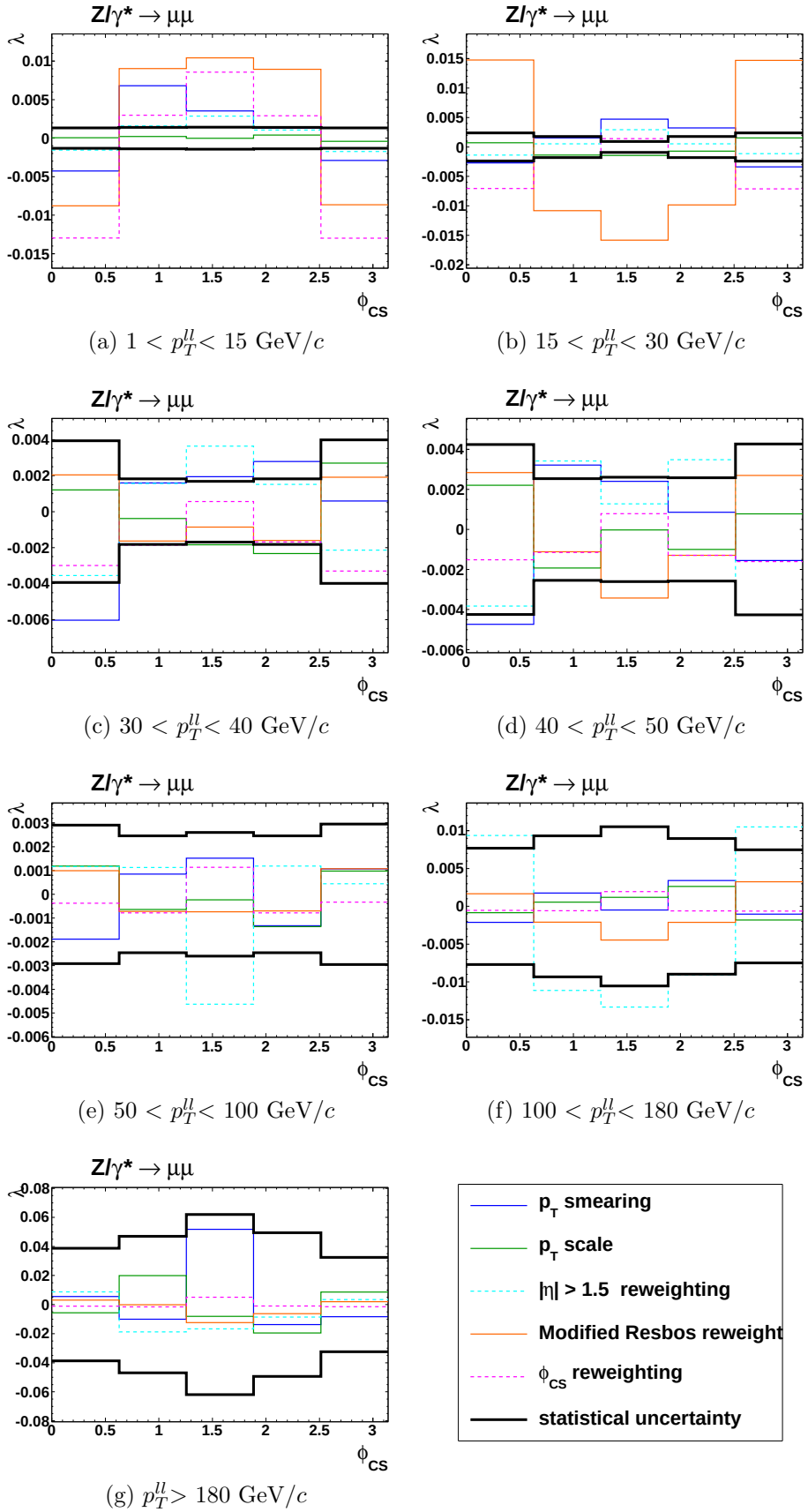

(a) $1 < p_T^{ll} < 15$ GeV/c

(b) $15 < p_T^{ll} < 30$ GeV/c

(c) $30 < p_T^{ll} < 40$ GeV/c

(d) $40 < p_T^{ll} < 50$ GeV/c

(e) $50 < p_T^{ll} < 100$ GeV/c

(f) $100 < p_T^{ll} < 180$ GeV/c

(g) $p_T^{ll} > 180$ GeV/c

Figure 6.9: Ratio of |smeared or reweighted correction factor - nominal correction factor| to nominal correction factor for dimuon events.

To calculate the total uncertainty on the corrected data the statistical uncertainties for each bin of the data ϕ_{CS} distribution are combined with the total uncertainty on the correction factor for that bin, where the total uncertainty on the correction factor is calculated as the quadrature sum of the differences between the nominal correction factor and each smeared or reweighted sample correction factor.

Chapter 7

Data and Monte Carlo Comparisons

Nominal correction factors are applied to the $\phi_{\rm CS}$ distributions for D0 Run II dielectron and dimuon data samples. The corrected data $\phi_{\rm CS}$ distributions are then plotted with their estimated combined uncertainties

The plots in this section show the $\phi_{\rm CS}$ distributions for corrected data compared to generator level PYTHIA MC with the total uncertainty on the data shown.

The corrected data shows good agreement with the PYTHIA generator MC samples for both the dielectron and dimuon analyses within the estimated uncertainties, up to $p_T^{ll} \approx 100$ GeV/c where available statistics are diminished.

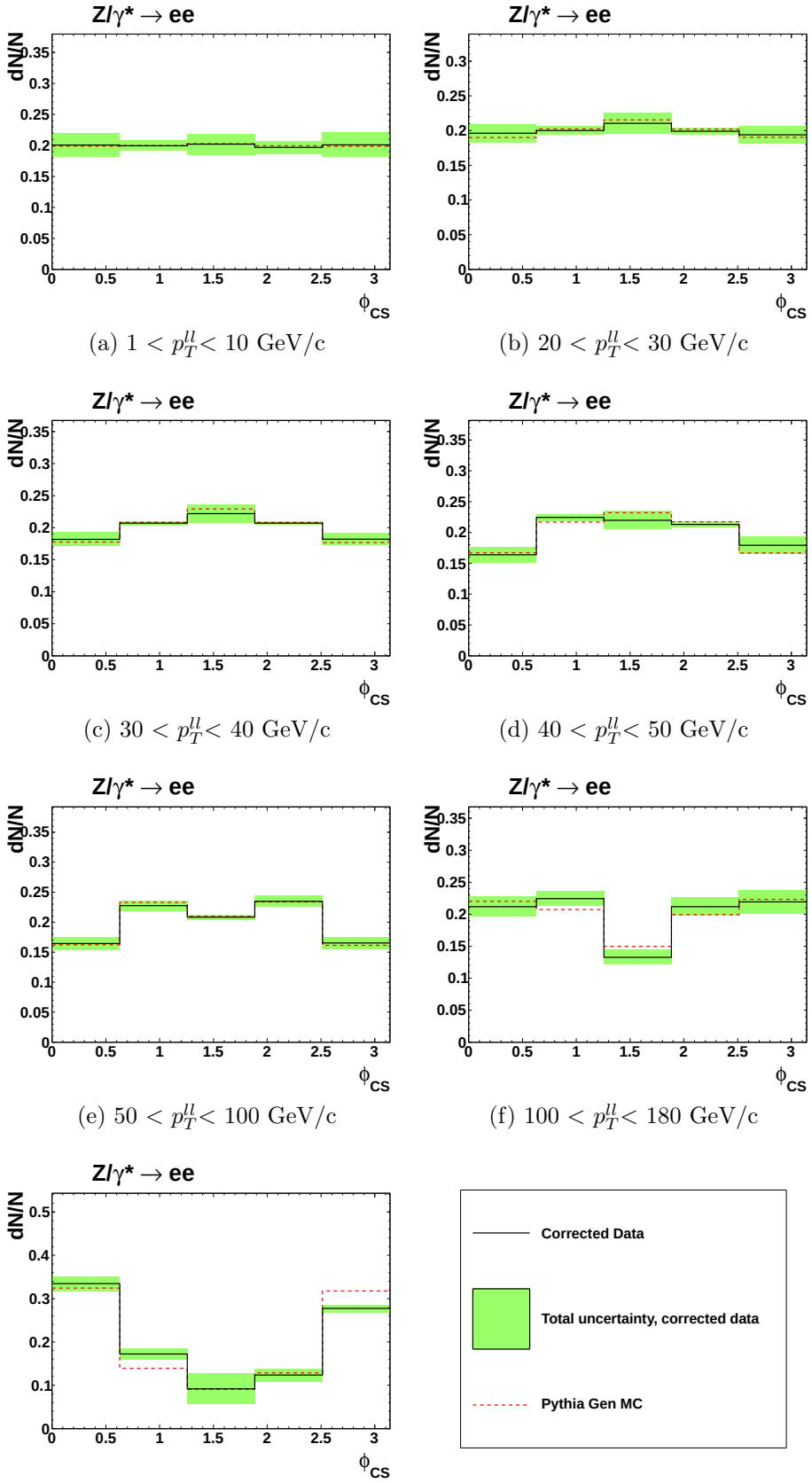

(a) $1 < p_T^{ll} < 10$ GeV/c

(b) $20 < p_T^{ll} < 30$ GeV/c

(c) $30 < p_T^{ll} < 40$ GeV/c

(d) $40 < p_T^{ll} < 50$ GeV/c

(e) $50 < p_T^{ll} < 100$ GeV/c

(f) $100 < p_T^{ll} < 180$ GeV/c

(g) $p_T^{ll} > 180$ GeV/c

Figure 7.1: Corrected dielectron data ϕ_{CS} distributions with estimated uncertainties compared to Pythia generator MC.

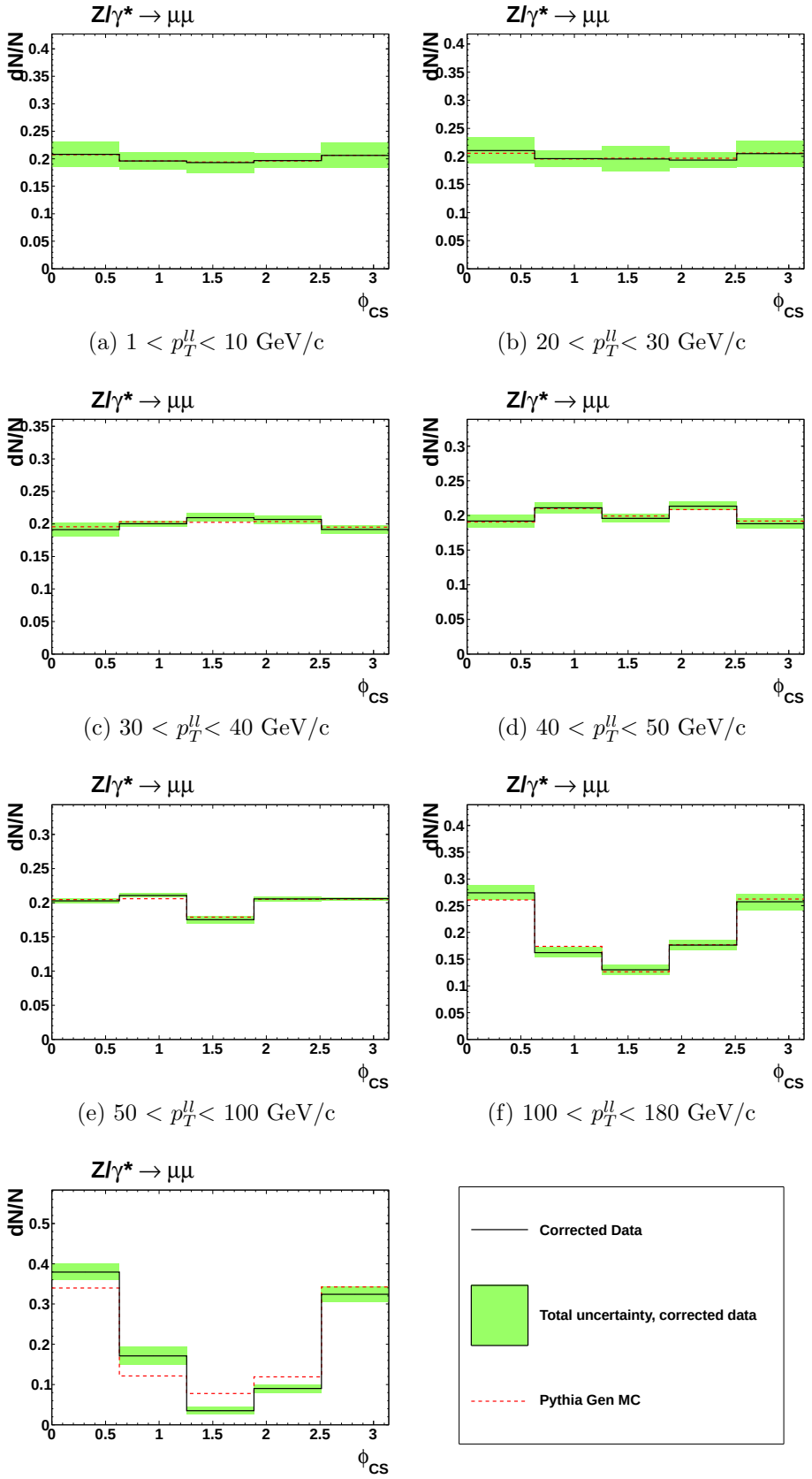

(a) $1 < p_T^{ll} < 10$ GeV/c

(b) $20 < p_T^{ll} < 30$ GeV/c

(c) $30 < p_T^{ll} < 40$ GeV/c

(d) $40 < p_T^{ll} < 50$ GeV/c

(e) $50 < p_T^{ll} < 100$ GeV/c

(f) $100 < p_T^{ll} < 180$ GeV/c

(g) $p_T^{ll} > 180$ GeV/c

Figure 7.2: Corrected dimuon data $\phi_{\rm CS}$ distributions with estimated uncertainties compared to Pythia generator MC.

Chapter 8

Conclusions

the aim of this analysis was to measure the distribution of ϕ_{CS} for Drell-Yan events in both dielectron and dimuon channels for 8.6 fb^{-1} of D0 Run II data. Reweightings and corrections were made to improve Monte Carlo simulation samples at generator and detector level. Selection requirements were made to eliminate backgrounds to provide a high purity signal dominated sample of events. ϕ_{CS}distributions for generator and detector level MC were compared and bin-by-bin correction factors to be applied to data were calculated. The systematic uncertainties for these correction factors were estimated by applying a range of smearings and reweightings and measuring their effects on the value of the measured correction factors. finally these correction factors were applied to detector data and the corrected ϕ_{CS} distributions were compared to generator level MC.

The estimated uncertainties on the final distributions of ϕ_{CS} are over conservative indicating that a simple bin-by-bin correction for the data ϕ_{CS} distribution is too crude a method to accurately compare detector data to generator level simulations for this variable.

8.1 Future Improvements

Before it would be possible for this analysis to be published for peer review further improvements would have to be made.

To improve the reduction of systematic uncertainties from the final ϕ_{CS} distributions, a more sophisticated method than a bin-by-bin correction factor is required to correct the data to match the generator level MC distribution. An example of a possibly improved method for observing the generator level ϕ_{CS} distribution in data is outlined in [12].

Comparison of data to other generator level MC samples should be made but only for MC events with the same settings, specifically that all MC generators have final state photons merged back into electron measurement or they all do not.

Bibliography

[1] S. D. Drell and T-M. Yan, *Massive lepton-pair production in hadron-hadron collisions at high energies*, Phys. Rev. Lett. 25, 316, 1970; Ann. Phys. (N.Y.) 66, 578, 1971

[2] J. C. Collins and D. E. Soper, *Angular distribution of dileptons in high-energy hadron collisions*, Phys. Rev. D 16, 2219, 1977

[3] D0 collaboration, *The D0 Detector*, Nucl. Instrum. Methods in Phys. Res. Sect. A 338, 185, 1994

[4] D0 collaboration, *The Upgraded D0 Detector*, Nucl. Instrum. Methods in Phys. Res. Sect. A 565, 463, 2006

[5] T. Sjöstrand *et al.*, *High-energy-physics event generation with Pythia 6.1*, Computer Physics Communications. 135, 238, 2001

[6] F. Landry *et al.*, Phys. Rev. D67 073016, 2003

[7] G. Corcella, I.G. Knowles, G. Marchesini, S. Moretti, K. Odagiri, P. Richardson, M.H. Seymour and B.R. Webber, *HERWIG 6.5*, JHEP 0101 010, 2001

[8] S. Alioli, P. Nason, C. Oleari, E. Re, *Vector boson plus one jet production in POWHEG*, JHEP 1101:095, 2011.

[9] S. Agostinelli *et al.*, GEANT 4 collaboration, GEANT *4 - a simulation toolkit*, Nuclear Instruments and Methods in Physics Research A 506 250-303, 2003

[10] P. Nadolwsky *et al.*, *Implications of CTEQ global analysis for collider observables*, Phys.Rev.D78:013004, 2008

[11] J. Pumplin *et al.*, *New Generation of Parton Distributions with Uncertainties from Global QCD Analysis* JHEP07 012 2002

[12] P. C. Hansen, *The L-curve and Its Use in the Numerical Treatment of Inverse Problems* Computational Inverse Problems in Electrocardiology, ed. P. Johnston, Advances in Computational Bioengineering, 2000